








## Article

# Corrosion Behavior of Titanium Alloys (Ti CP2, Ti-6Al-2Sn-4Zr-2Mo, Ti-6Al-4V and Ti Beta-C) with Anodized and Exposed in NaCl and H<sub>2</sub>SO<sub>4</sub> Solutions

Citlalli Gaona-Tiburcio <sup>1</sup>, Jesús Manuel Jáquez-Muñoz <sup>1,2,\*</sup>, Demetrio Nieves-Mendoza <sup>3</sup>, Erick Maldonado-Bandala <sup>3</sup>, Maria Lara-Banda <sup>1</sup>, Manuel Alejandro Lira-Martinez <sup>2</sup>, Hortensia Reyes-Blas <sup>2</sup>, Miguel Ángel Baltazar-Zamora <sup>3</sup>, Laura Landa-Ruiz <sup>3</sup>, Luis Daimir Lopez-Leon <sup>4</sup> and Facundo Almeraya-Calderon <sup>1,\*</sup>

- <sup>1</sup> FIME, Centro de Investigación e Innovación en Ingeniería Aeronáutica (CIIA), Universidad Autónoma de Nuevo León, San Nicolás de los Garza 66455, Mexico; citlalli.gaonatbr@uanl.edu.mx (C.G.-T.); maria.laraba@uanl.edu.mx (M.L.-B.)
- <sup>2</sup> Instituto de Ingeniería y Tecnología, Universidad Autónoma de Ciudad Juárez, Ciudad Juárez 32310, Mexico; manuel.lira@uacj.mx (M.A.L.-M.); hortensia.reyes@uacj.mx or hortensia.reyes@uv.mx (H.R.-B.)
- <sup>3</sup> Facultad de Ingeniería Civil, Universidad Veracruzana, Xalapa 91000, Mexico; dnieves@uv.mx (D.N.-M.); erimaldonado@uv.mx (E.M.-B.); mbaltazar@uv.mx (M.Á.B.-Z.); lalanda@uv.mx (L.L.-R.)
- <sup>4</sup> Área Académica de Ingeniería y Arquitectura, Universidad Autónoma del Estado de Hidalgo, Carretera Pachuca-Tulancingo, Km 4.5, Pachuca 42082, Mexico; olguinc@uaeh.edu.mx or luis\_lopez@uaeh.edu.mx
- \* Correspondence: jesus.jaquezmn@uanl.edu.mx (J.M.J.-M.); facundo.almerayaald@uanl.edu.mx (F.A.-C.)



**Citation:** Gaona-Tiburcio, C.; Jáquez-Muñoz, J.M.; Nieves-Mendoza, D.; Maldonado-Bandala, E.; Lara-Banda, M.; Lira-Martinez, M.A.; Reyes-Blas, H.; Baltazar-Zamora, M.Á.; Landa-Ruiz, L.; Lopez-Leon, L.D.; et al. Corrosion Behavior of Titanium Alloys (Ti CP2, Ti-6Al-2Sn-4Zr-2Mo, Ti-6Al-4V and Ti Beta-C) with Anodized and Exposed in NaCl and H<sub>2</sub>SO<sub>4</sub> Solutions. *Metals* **2024**, *14*, 160. <https://doi.org/10.3390/met14020160>

Academic Editor: Renato Altobelli Antunes

Received: 4 January 2024

Revised: 26 January 2024

Accepted: 26 January 2024

Published: 28 January 2024



**Copyright:** © 2024 by the authors. Licensee MDPI, Basel, Switzerland. This article is an open access article distributed under the terms and conditions of the Creative Commons Attribution (CC BY) license (<https://creativecommons.org/licenses/by/4.0/>).

**Abstract:** Nowadays, different industries, such as the aerospace and biomedical industries, prefer using Ti alloys due to their excellent anti-corrosion properties and ability to generate a TiO<sub>2</sub> oxide layer; this induces the use of anodization to increase the useful life of components. The aim of this work is to characterize the electrochemical effect of anodizing treatment on titanium alloys (Ti CP2, Ti-6Al-2Sn-4Zr-2Mo, Ti-6Al-4V, and Ti Beta-C) in NaOH and KOH at 1 M, applying a current density of 0.0025 A/cm<sup>2</sup>. The electrochemical techniques employed were electrochemical noise (EN) and electrochemical impedance spectroscopy (EIS), supported by ASTM G199 and ASTM G106 in electrolytes of NaCl and H<sub>2</sub>SO<sub>4</sub> at 3.5 wt. % as a simulation of marine and industrial atmospheres. Also, the anodized transversal section and surface morphology were characterized by a scanning electron microscope (SEM). The results of both electrochemical techniques indicated that Ti-6Al-2Sn-4Zr-2Mo anodized in NaOH presented the best properties against corrosion, and the thickness of the oxide was the biggest.

**Keywords:** titanium; anodized; alkaline; electrochemical noise; Hilbert–Huang recurrence plots; electrochemical impedance spectroscopy

## 1. Introduction

The aerospace, biomedical, chemical, naval, and automotive industries need materials with special anti-corrosion properties due to their high performance. Therefore, titanium and its alloys have been considered an option for those industries [1–3].

Considering that titanium is a very reactive material, even when exposed to oxygen, it generates an oxide layer, mostly of TiO<sub>2</sub>, depending on the alloying element. The generation of the oxide layer increases the resistance against alloy corrosion. However, the quality of the oxide layer will depend on the chemical composition of the alloy and factors such as area, roughness, and material porosity. Other important factors are the oxygen in the system, the humidity, and the environmental composition [4–9].

A good generation of a passive layer has many variables; for that reason, titanium and its alloys are susceptible to attacks in different electrolytes because of irregular passive layer formation. The predisposition of titanium to generate a natural oxide layer makes

it perfect for being anodized. Authors have reported that anodized titanium generates a bigger oxide layer than passivated titanium, making it more corrosion-resistant. Also, they reported a homogeneous morphology, good thermodynamic stability, low conductivity, and low ion formation [10–14].

The anodized process consists of two different stages. The first is generating a constant oxide layer, which occurs quickly when applying a current. The next stages consist of the porous layer generation, increasing the thickness of the coating. The anodization process occurs due to a diffusion of oxygen and titanium on the surface; metal ions move to the interface of anodization through oxygen adsorption, generating  $\text{TiO}_2$  on the surface [15,16].

However, the homogeneity of the oxide layer will depend on anodization factors such as pH, current, oxygen in the system, electrolytes, and the chemical composition of the Ti alloy. Usually, acid electrolytes are employed as anodizing bath solutions; however, authors such as Hugot-Le Goff [17] report that anodizing in basic media generates good oxide layers. Afshar and Veazi [18] reported an anodizing thickness from 0.4 to 1.5  $\mu\text{m}$  when a Ti CP1 was anodized in NaOH, varying the anodizing time. In both cases, the corrosion resistance increased and was related to the high concentration of NaOH with a compact and homogenous coating. Also, they reported differences between anodized alloys obtained by acid media, mainly  $\text{H}_2\text{SO}_4$  and  $\text{H}_3\text{PO}_4$  [19].

It is important to mention that anodizing has several advantages compared to other coating methods. Thermal oxidation, sputtering, passivation, electrodeposition, and sol-gel generate an oxide layer in Ti and Ti alloys. Still, this method presents disadvantages such as high costs, difficult application for complex geometries, and the lack of homogeneous oxide generated.

The aim of this work is to characterize the electrochemical effect of anodizing treatment on titanium alloys (Ti CP2, Ti-6Al-2Sn-4Zr-2Mo, Ti-6Al-4V, and Ti Beta-C) in NaOH and KOH electrolytes. The electrochemical techniques employed were electrochemical noise (EN) and electrochemical impedance spectroscopy (EIS), with the anodized alloys exposed to NaCl and  $\text{H}_2\text{SO}_4$  solutions at 3.5 wt. %, simulating marine and industrial atmospheric conditions.

## 2. Materials and Methods

### 2.1. Materials

The materials employed were Ti CP2, Ti-6Al-2Sn-4Zr-2Mo, Ti-6Al-4V, and Ti Beta-C, used in the received condition. Table 1 shows the chemical composition of these alloys obtained by X-ray fluorescence (Olympus DELTA XRF, Houston, TX, USA).

**Table 1.** Chemical composition of Ti and its alloys (wt. %).

Elements	Ti CP2	Alloys		
		Ti-6Al-2Sn-4Zr-2Mo	Ti-6Al-4V	Ti Beta-C
Fe	0.038 ± 0.005	–	0.21 ± 0.01	0.08 ± 0.01
Al	–	6.75 ± 0.20	7.14 ± 0.37	4.2 ± 0.13
V	–	–	4.03 ± 0.08	8.1 ± 0.07
Zr	–	4.18 ± 0.01	–	4.3 ± 0.01
Cr	–	–	–	3.3 ± 0.07
Mo	–	1.99 ± 0.008	–	3.9 ± 0.01
Sn	–	2.08 ± 0.01	–	–
Ti	99.94 ± 0.005	84.65 ± 0.19	87.71 ± 0.36	75.2 ± 0.14

### 2.2. Anodized Treatment

The alloys were pretreated for 10 min in an ultrasonic cleaner with ethanol and deionized water. The anodized treatment employed a platinum mesh as a cathode, and the

NaOH and KOH electrolytes were used at 1 M concentration. The anodized temperature was  $25\text{ }^{\circ}\text{C} \pm 1$  [analytical grade reagents (JT Baker)]. The power source was the XLN300025-GL, applying a current density of  $2.5 \times 10^{-3}\text{ A/cm}^2$ . The anodizing time was 10 min, and the standards employed were AMS2487B and AMS2488E [20,21].

### 2.3. Microstructural Characterization

The Ti and Ti alloys were prepared employing the metallographic technique. The materials were brazed with SiC sandpaper grade 800. All the samples were cleaned for 10 min in ethanol and deionized water by ultrasonic cleaning [22].

The surface and cross-section of anodized alloys were studied using secondary electron (SE) and backscattered electron (BSE) detectors in a scanning electron microscope (SEM, Hitachi, Tokyo, Japan) operating at 20 kV, with an 8.5 and 12 mm work distance.

### 2.4. Corrosion Measurements

Electrochemical noise (EN) and electrochemical impedance spectroscopy (EIS) were performed at room temperature, using VersaSTAT4 Princeton Applied Research software (Ametek, Inc., Oak Ridge, TN, USA), in 3.5 wt. % NaCl and  $\text{H}_2\text{SO}_4$  electrolytes at room temperature and all the corrosion tests were performed in duplicate. The cell configuration was of three electrodes: the working electrode (WE), the reference of the saturated calomel electrode (SCE), and the counter electrode (CE) of platinum. The area exposed was  $1\text{ cm}^2$  [23]. For the EN technique, we acquired 4096 data points, at 1 datum per second, and the signal was processed with MATLAB 2018a [24]. EIS measurements were recorded at the corrosion potential over a frequency range from 100 kHz to 10 mHz, obtaining 10 points per decade, and applying an AC potential signal at 10 mV (root mean square, rms) amplitude according to the ASTM G106-15 standard. The results were interpreted through the development of typical impedance models for the electrode surface, as well as curve fitting based on an equivalent circuit using the Zview Impedance program. The time to obtain the steady state was 50 min in an open circuit.

## 3. Results

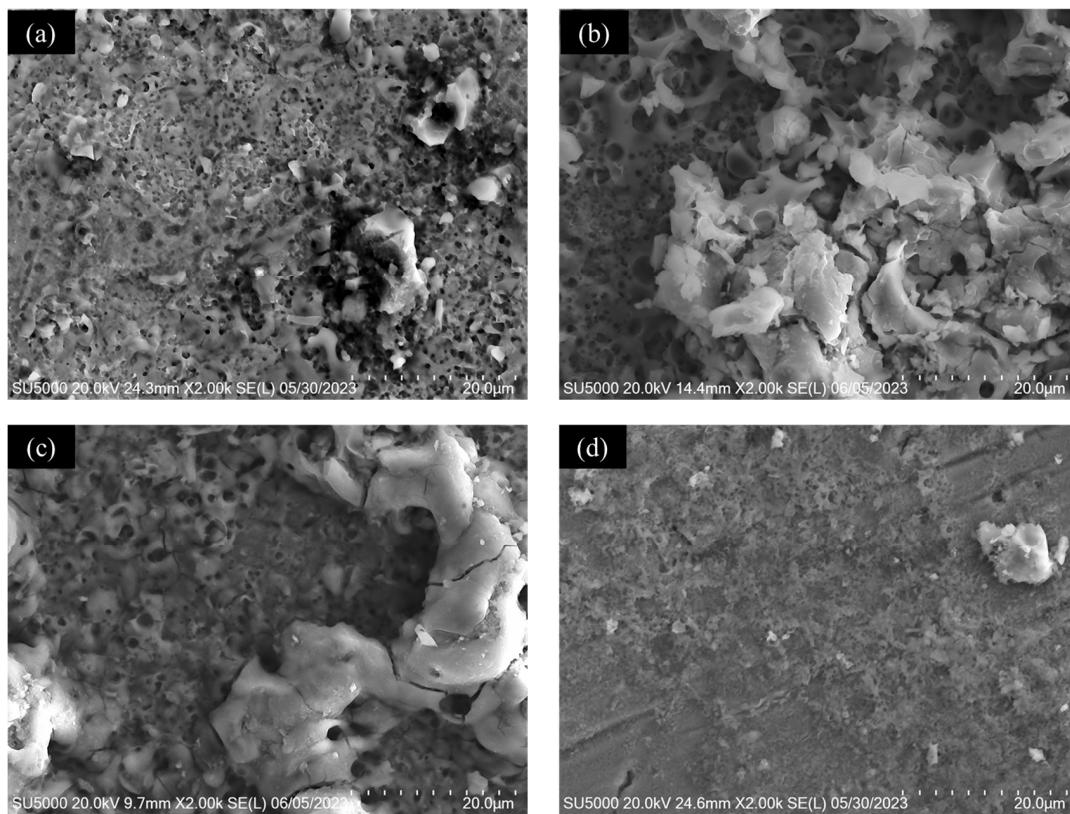
### 3.1. Microscopic Characterization

Figure 1 shows the superficial morphology of anodized alloys in NaOH obtained by SEM-SE. In this anodizing electrolyte, the oxide distribution is heterogeneous. Figure 1b shows the preferential oxide deposition, where Ti-6Al-2Sn-4Zr-2Mo presented different altitudes. Also, the anodized alloy presented cracking in that zone. A similar morphology is observed in Figure 1c, presenting a preference for the accumulation of oxide in specific areas. The anodizing shown in Figure 1d, corresponding to Ti Beta-C, shows low coating generation.

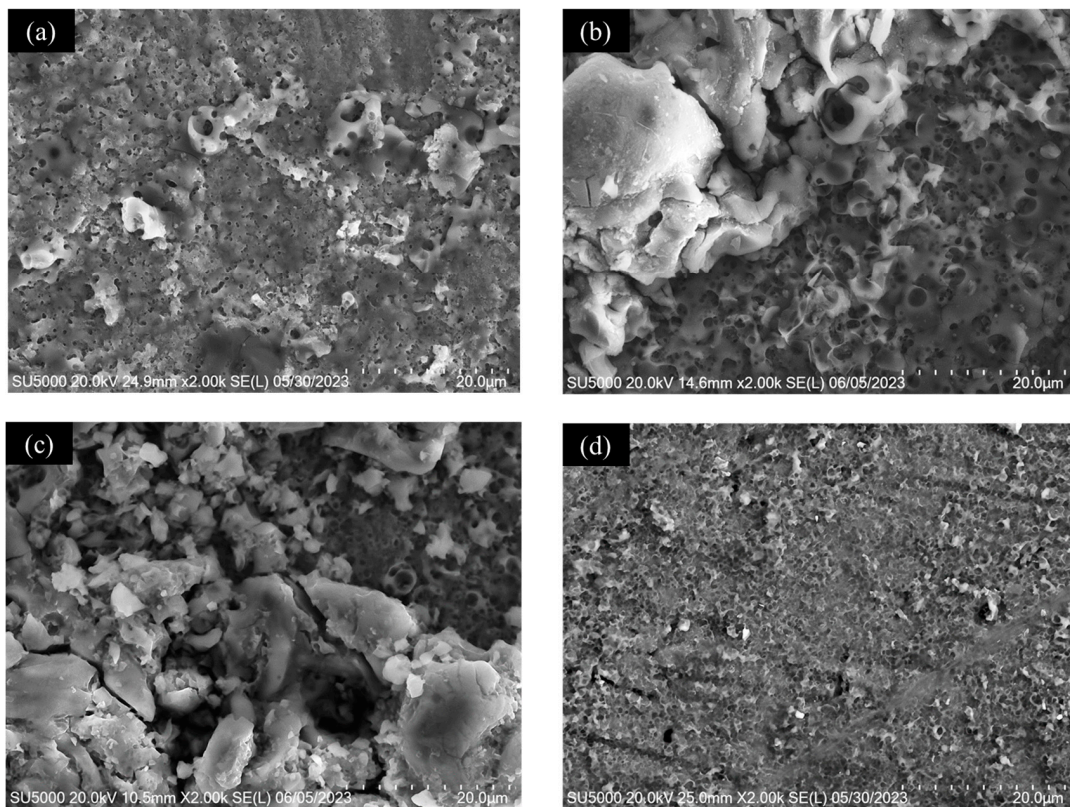
Figure 2 shows the micrographics of anodized alloys in KOH. When alloys were anodized in KOH, they presented a higher heterogeneity than in NaOH; in Figure 2a, the anodized Ti CP2 presents different altitudes of oxide. A similar behavior is observed in Figure 2d for Ti Beta-C, but the polish lines are higher. Figure 2b,c presents similar behavior, with a higher anodized generation, but it continues to be non-homogenous.

Figure 3 shows the transversal section of anodized alloys in NaOH. Figure 3a shows the transversal section of Ti CP2, where the anodized alloy presented a thickness of 376 to 400 nm, and the mapping shows the presence of O and an increase in the oxide layer. Ti-6Al-2Sn-4Zr-2Mo presented a higher thickness, with values from 1.92 to 2.63  $\mu\text{m}$ ; the presence of O and Ti in the oxide layer is higher (see Figure 3b). On the other hand, Figure 3c shows the anodized alloy of Ti-6Al-4V, which presented lower values, with thicknesses from 23 to 25 nm. Finally, Figure 3d shows the anodization of Ti Beta-C, where the thickness obtained was 660 and 756 nm; the mapping shows the presence of oxygen in the coating zone. Only the anodized version of Ti-6Al-2Sn-4Zr-2Mo meets the requirements of AMS2487B specifications.





**Figure 1.** SEM-SE of superficial morphology of anodized in NaOH in 2000 $\times$ ; (a) Ti CP2, (b) Ti-6Al-2Sn-4Zr-2Mo, (c) Ti-6Al-4V y (d) Ti Beta C.



**Figure 2.** SEM-SE of superficial morphology of anodized in KOH in 2000 $\times$ ; (a) Ti CP2, (b) Ti-6Al-2Sn-4Zr-2Mo, (c) Ti-6Al-4V y (d) Ti Beta C.



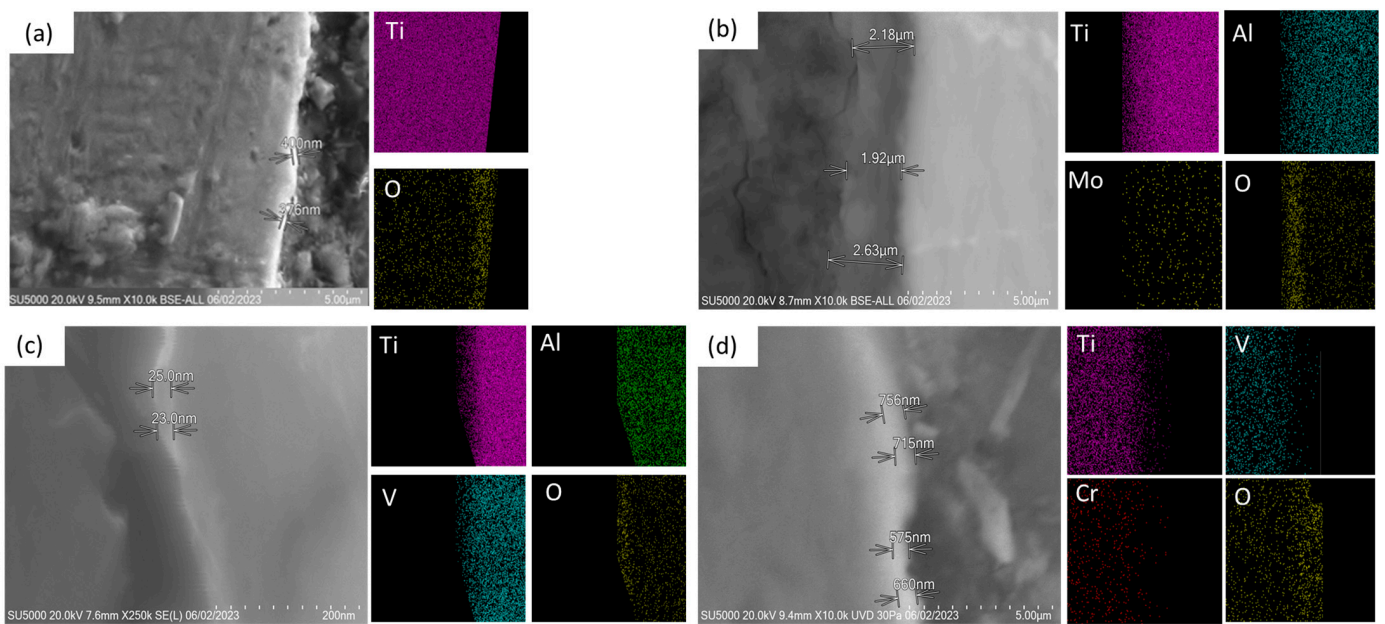


**Figure 3.** SEM-SE/BSE of transversal section of anodized titanium alloys in NaOH at 10,000 $\times$ , and element mapping by EDS of (a) Ti CP2, (b) Ti-6Al-2Sn-4Zr-2Mo, (c) Ti-6Al-4V y (d) Ti Beta C.

Figure 4 shows the transversal section of anodized alloys in KOH, where Ti CP2 presents a thickness from 2.1 to 2.7  $\mu\text{m}$ , being the highest in both anodizing electrolytes. Also, this layer presented acceptable adhesion characteristics to metal; however, the thickness is heterogeneous. Figure 4b shows the anodization of Ti-6Al-2Sn-4Zr-2Mo, where the thickness varies from 1.02 to 2.02  $\mu\text{m}$  and is non-homogenous. The mapping presented a greater presence of oxygen in the anodized layer. Figure 4c presents a thickness from 208 to 248 nm, and the thickness of Figure 4d ranges from 525 to 1.03  $\mu\text{m}$  (see Table 2). All the anodized alloys presented oxygen in the coating. In this case, only the anodized Ti CP2 and Ti-6Al-2Sn-4Zr-2Mo satisfied the AMS2487B specifications.

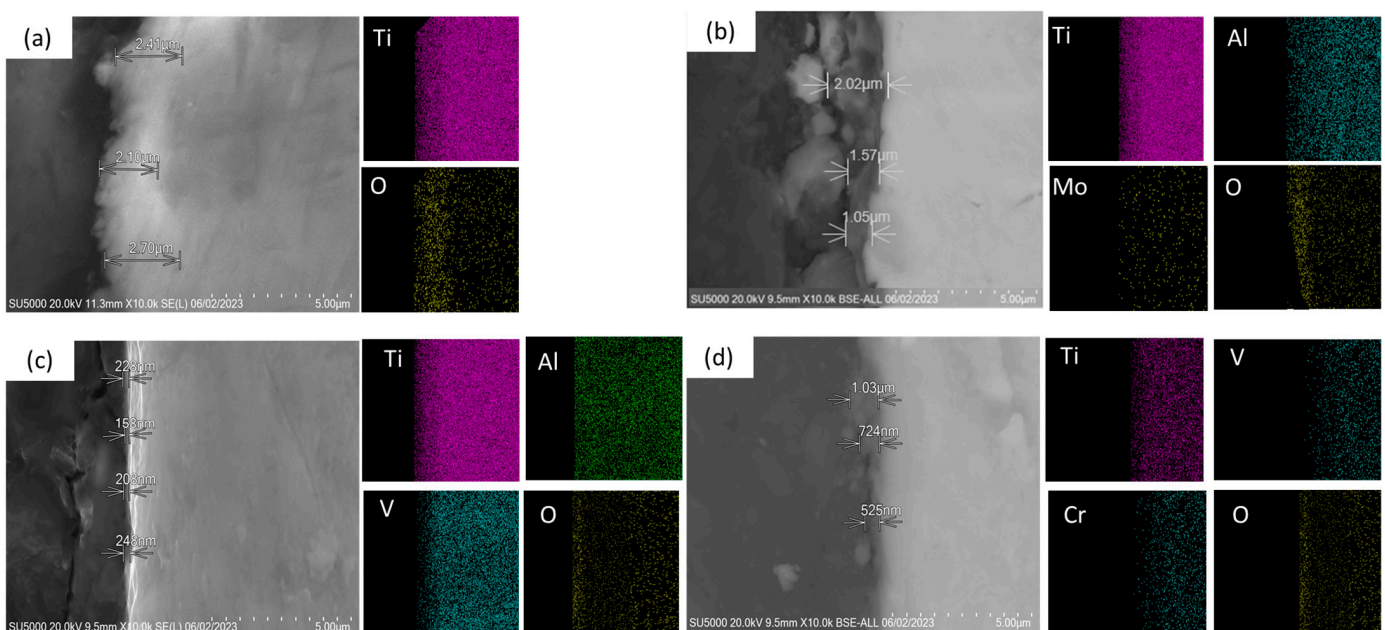


**Figure 4.** SEM-SE/BSE of transversal section of anodized titanium alloys in KOH at 10,000 $\times$ , and element mapping by EDS of (a) Ti CP2, (b) Ti-6Al-2Sn-4Zr-2Mo, (c) Ti-6Al-4V y (d) Ti Beta C.

**Table 2.** Thicknesses of anodized titanium alloys.

Alloy	Electrolyte	Average Thickness ( $\mu\text{m}$ )
Ti CP2	NaOH	0.45
	KOH	2.4
Ti-6Al-2Sn-4Zr-2Mo	NaOH	2.45
	KOH	1.5
Ti-6Al-4V	NaOH	0.024
	KOH	0.2
Ti Beta-C	NaOH	0.67
	KOH	0.75

### 3.2. Electrochemical Noise

#### 3.2.1. Hilbert–Huang Transform (HHT)

The electrochemical noise (EN) technique describes the electrochemical phenomenon that occurs during the corrosion process. One method to characterize the EN technique is Hilbert–Huang analysis. This method helps the frequency and time in which an energy interchange occurs; the energy is called instantaneous energy and is obtained by the decomposition of the signal obtained by the intrinsic function of the signal [25–30]. The empirical method of decomposition (EMD) can be explained by the Equation (1):

$$x(t) = \sum_{i=1}^N h^{(i)}(t) + d(t) \quad (1)$$

where  $d(t)$  is the average of the trend at a low frequency of the time series  $x(t)$  and cannot be decomposed and  $h^{(i)}(t)$  is the  $i$ -th term of IMF that is generated. These numbers must satisfy the conditions that the extreme and cross numbers are equal or differ by a maximum of 1 and that each point using the local maximum and minimum must be 0. The HHT is represented by Equation (2):

$$y_j(t) = \frac{1}{\pi} p \int_{-\infty}^{\infty} \frac{h_j(\tau)}{t - \tau} d\tau \quad (2)$$

where  $y_j(t)$  is the Hilbert transform and IMF is represented with  $h_j$ ;  $p$  is related to the Cauchy principle and is linked with an average of IMF.

Figure 5 shows the behavior of Ti alloys anodized in NaOH when analyzed using the HHT method. All the alloys anodized shown in that figure demonstrate the same pattern: the presence of energy in middle and low frequencies, with high energy at middle frequencies. This behavior is related to non-homogenous anodization on the surface, but a protective layer is present due to energy at a low frequency. The only anodized alloy that presented energy at high frequencies is Ti Beta-C, anodized in  $\text{H}_2\text{SO}_4$ , in Figure 5h, meaning that the anodized alloy is weak in the presence of the acid media. The high energy at middle frequencies means that the ions first attack preference zones of the anodized surface. However, after time passes, the energy decreases and is accumulated at low frequencies due to the accumulation of those ions on the surface.

Figure 6 shows the Hilbert specters of Ti alloys anodized in KOH in both media. The anodized Ti CP2 of Figure 6a,b presents energy at high and middle frequencies, even in NaCl and  $\text{H}_2\text{SO}_4$ ; irregular behavior is associated with a heterogeneous anodized alloy. The energy at low frequencies in Figure 6b indicates the ions' accumulation on the surface. Figure 6c–f for Ti-6Al-2Sn-4Zr-2Mo and Ti-6Al-4V showed a more homogenous anodized alloy than Ti CP2 and Ti Beta-C. The anodized Ti Beta-C presented high instability in both media when exposed to NaCl (Figure 6g). The anodized alloy showed high energy accumulation at high frequencies in all the time series, indicating that it is heterogeneous

and that ions attack in preferential zones. Figure 6h shows a similar behavior, but the presence of energy is not higher than in Figure 6g; this occurs due to the susceptibility of anodized alloys to  $\text{Cl}^-$  ions.

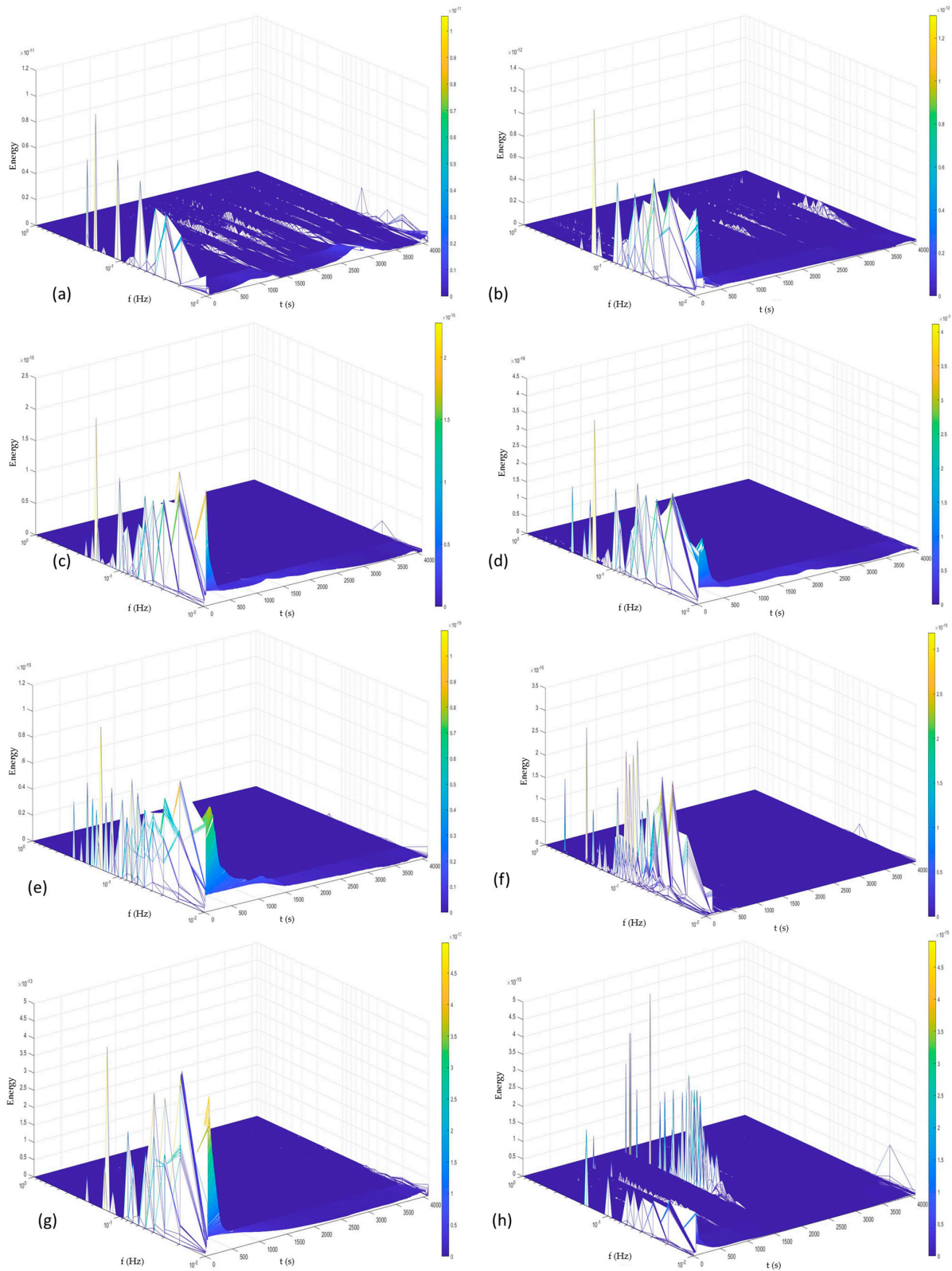


**Figure 5.** Hilber specter for anodized titanium alloys in NaOH in NaCl (left) and  $\text{H}_2\text{SO}_4$  (right) of Ti CP2 (a,b), Ti-6Al-2Sn-4Zr-2Mo (c,d), Ti-6Al-4V (e,f), and Ti Beta-C (g,h).



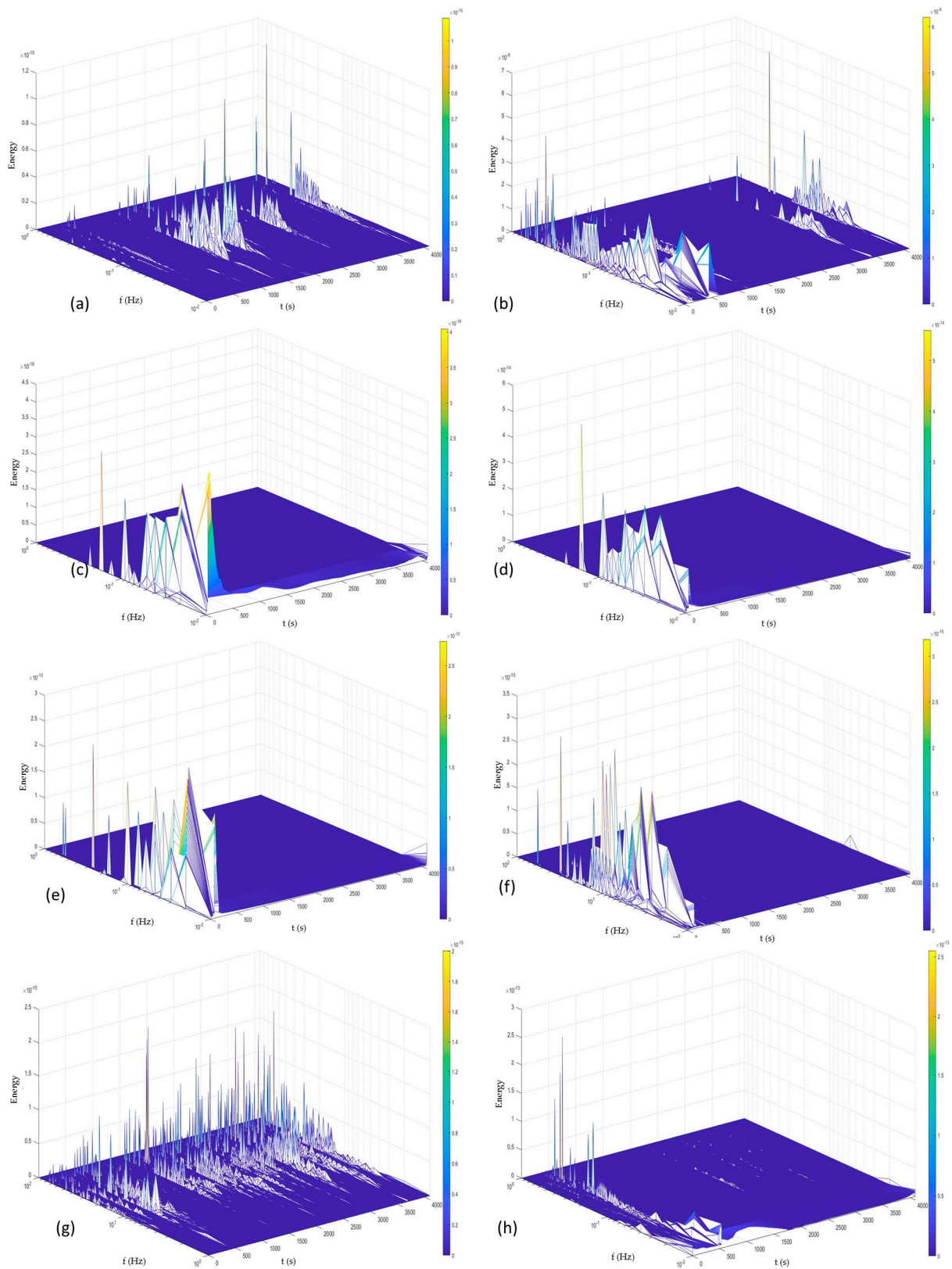


**Figure 6.** Hilber specter for anodized titanium alloys in KOH in NaCl (left) and  $H_2SO_4$  (right) of Ti CP2 (a,b), Ti-6Al-2Sn-4Zr-2Mo (c,d), Ti-6Al-4V (e,f), and Ti Beta-C (g,h).

### 3.2.2. Recurrence Plots Analysis (RP)

Recurrence plots are helpful tools for analyzing non-linear systems. As corrosion is a chaotic and non-linear system, it is necessary to employ different techniques to evaluate the corrosion type and process on the surface. RP is an excellent technique with which to conduct that analysis.

Recurrence plots are two-dimensional diagrams that are realized in time function. The trajectory of  $x_i \in R^m$ , where a dimension (m) of space is prescribed at a time limit of  $\varepsilon$  to  $i$  and  $j$ . The RP visualizes a two-dimensional square matrix from two dimensions with the times  $t_i$  and  $t_j$ . Equation (3) shows the matrix [31–34]:

$$R_{ij}(\varepsilon) = \Theta \left( \varepsilon - \left\| \vec{x}_i - \vec{x}_j \right\| \right), \quad i, j = 1, \dots, N \quad (3)$$

where  $N$  is the number of data or points  $x_i$ ,  $\varepsilon$  is the distance umbral,  $\Theta(x)$  is the Heaviside function, and  $\| \cdot \|$  is the norm (Euclidean, maximum, or Manhattan).

The recurrence density is determined by the recurrence rate that Equation (4) shows:

$$RR(\varepsilon) = \frac{1}{N^2} \sum_{i, j=1}^N R_{i, j} \quad (4)$$

The recurrence rate (RR) gives the probability of reconstruction of one trajectory in an umbral zone.

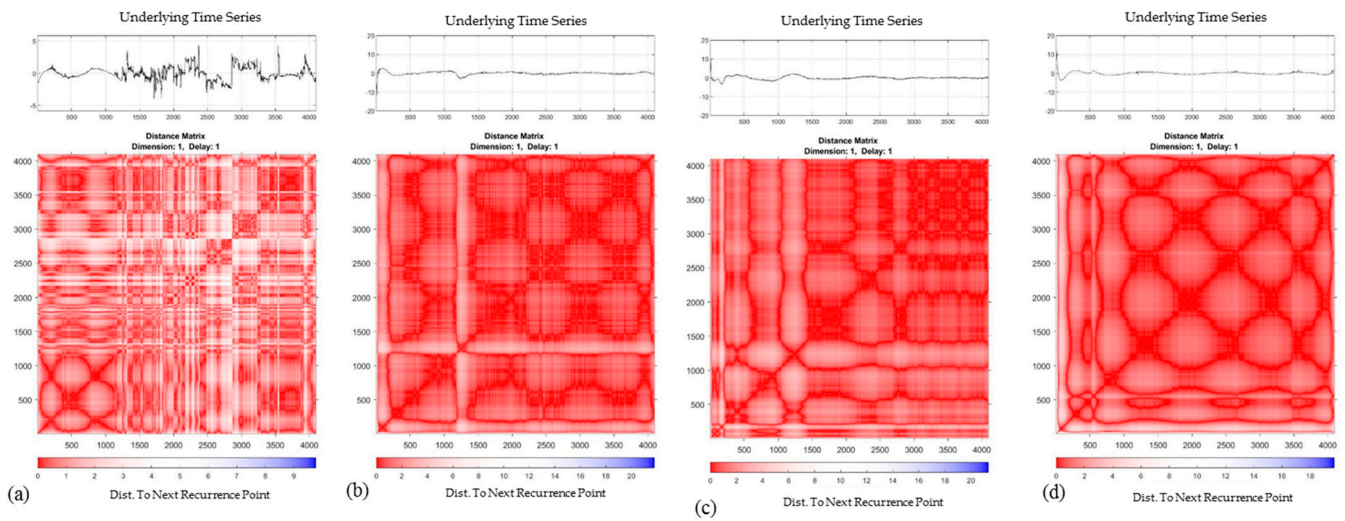
The diagonal lines of RP represent the evolution of the trajectory in the space of the phase on different occasions and indicate the system's determinism. The determinism (DET) is calculated by the next equation:

$$DET = \frac{\sum_{l=l_{min}}^N l p(l)}{\sum_{l=1}^N l p(l)} \quad (5)$$

The laminarity is defined as the relation between the recurrence points in the vertical structures and the total number shown in Equation (6):

$$LAM = \frac{\sum_{v=v_{min}}^N v p(v)}{\sum_{v=1}^N v p(v)} \quad (6)$$

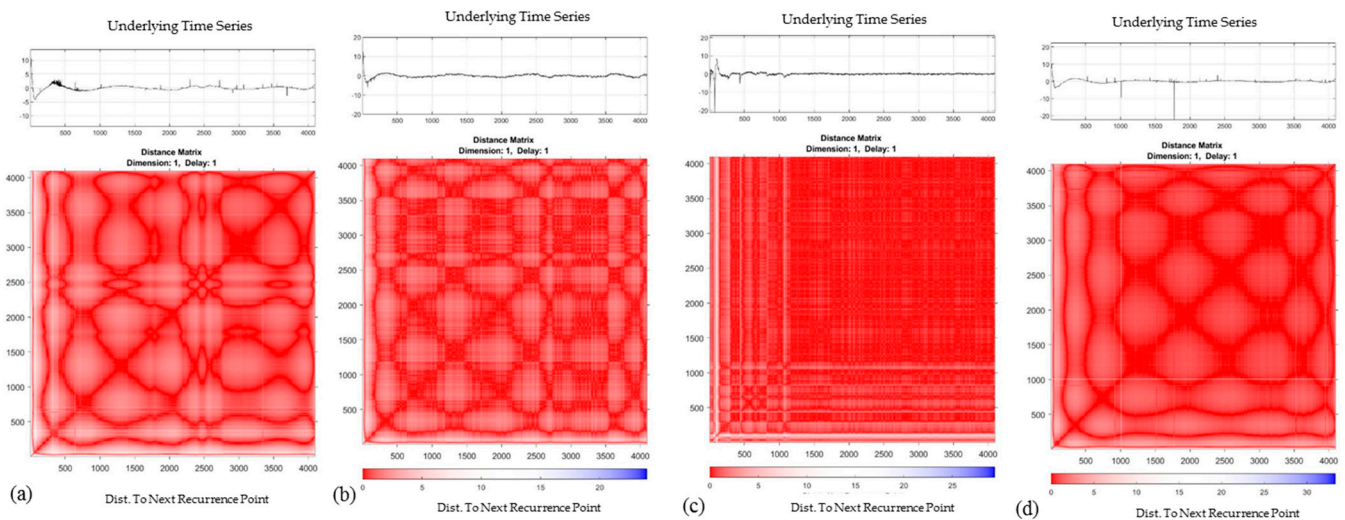
Figure 7 shows the anodized alloys' recurrence plots in NaOH when exposed to NaCl and H<sub>2</sub>SO<sub>4</sub>. When the anodized alloys are exposed to NaCl, as Figure 7a–d shows, they present different behaviors. The anodized Ti CP2 and Ti-6Al-4V presented less deterministic behavior (see Table 3), meaning that the exposed oxide layer is more susceptible to Cl ions. On the other hand, anodized Ti-6Al-2Sn-4Zr-2Mo and Ti Beta-C presented more deterministic behavior, with values between 0.8270 and 0.9697, indicating that the localized process is reduced. The alloys anodized in H<sub>2</sub>SO<sub>4</sub> are shown in Figure 8a–d; in this case, the anodized Ti-6Al-2Sn-4Zr-2Mo and Ti-6Al-4V (Figure 8b,c) presents low deterministic values, from 0.4723 to 0.5373, indicating that a localized process occurs at the surface; this is because horizontal and vertical lines decrease the laminarity of the system. The OH<sup>−</sup> ions attack the porous surface.



**Figure 7.** Recurrence plots of anodized titanium alloys in NaOH bath and exposed in NaCl for Ti CP2 (a), Ti-6Al-2Sn-4Zr-2Mo (b), Ti-6Al-4V (c) y Ti Beta-C (d).

**Table 3.** Parameters obtained of anodized titanium alloys in NaOH bath by Recurrence Plots analysis.

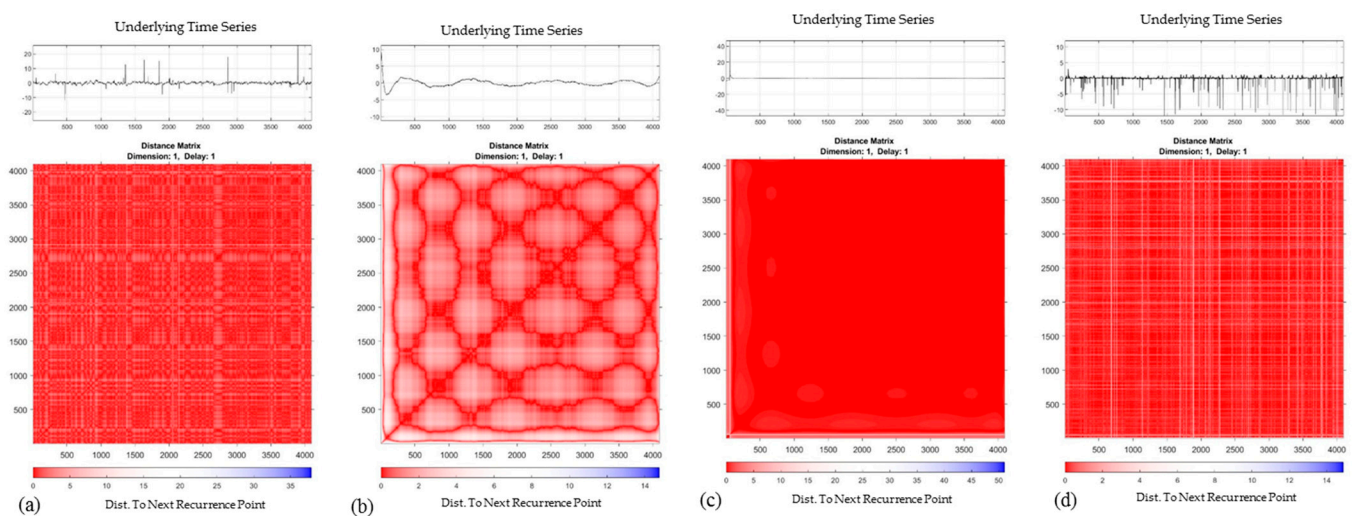
Anodized	Alloy	RR	DET	
NaOH		NaCl		
		Ti CP2	0.0671	0.6951
		Ti-6Al-2Sn-4Zr-2Mo	0.0927	0.827
		Ti-6Al-4V	0.0816	0.7368
		Ti Beta-C	0.0988	0.9697
			H <sub>2</sub> SO <sub>4</sub>	
		Ti CP2	0.0991	0.9155
		Ti-6Al-2Sn-4Zr-2Mo	0.0868	0.5373
	Ti-6Al-4V	0.1666	0.4723	
	Ti Beta-C	0.1088	0.9001	



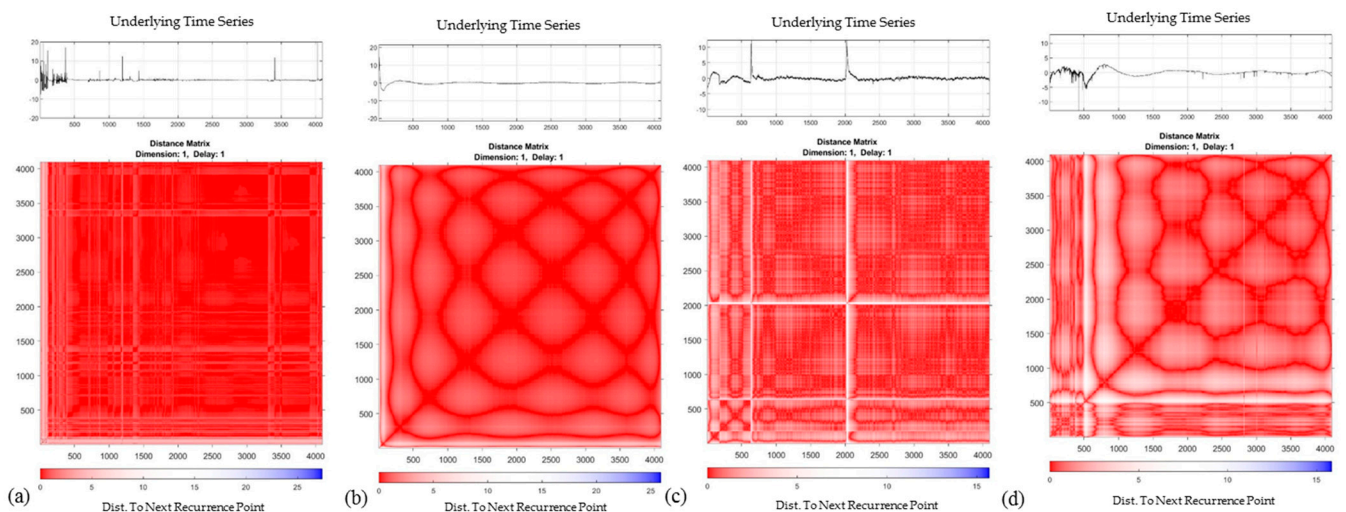
**Figure 8.** Recurrence plots of anodized titanium alloys in NaOH bath and exposed in and H<sub>2</sub>SO<sub>4</sub> for Ti CP2 (a), Ti-6Al-2Sn-4Zr-2Mo (b), Ti-6Al-4V (c) y Ti Beta-C (d).



Figure 9 shows the recurrence plots when alloys were anodized on KOH. The anodized exposure in NaCl (Figure 9a–d presents results of low determinism, especially for Ti CP2 and Ti Beta-C); this behavior is attributed to the great number of anodic and cathodic reactions occurring on the surface. Due to the low anodized quality in that medium and the susceptibility to  $\text{Cl}^-$  ions, the values of determinism are 0.5542 and 0.6901, respectively. The low determinism decreases the laminarity value to 0.7094 and 0.8070 for Ti CP2 and Ti Beta-C. The anodized Ti-6Al-2Sn-4Zr-2Mo and Ti-6Al-4V present a better performance in this media. When anodized surfaces are exposed to  $\text{H}_2\text{SO}_4$  (Figure 10a–d), Ti-6Al-4V showed the lowest deterministic value (0.4718) due to transients that reflect instability on anodized surfaces by anodic reactions. The anodized Ti Beta-C presents low determinism in the first seconds and at the end, with values of 0.8696 and 0.9285 of determinism and laminarity, respectively. When transients increase, the lines create cross-sections and decrease the laminarity and determinism (see Table 4).



**Figure 9.** Recurrence plots of anodized in a KOH bath and exposed in NaCl for Ti CP2 (a), Ti-6Al-2Sn-4Zr-2Mo (b), Ti-6Al-4V (c) y Ti Beta-C (d).



**Figure 10.** Recurrence plots of anodized in a KOH bath and exposed in  $\text{H}_2\text{SO}_4$  for Ti CP2 (a), Ti-6Al-2Sn-4Zr-2Mo (b), Ti-6Al-4V (c) y Ti Beta-C (d).

**Table 4.** Parameters obtained of anodized titanium alloys in a KOH bath by recurrence plots analysis.

Anodized	Alloy	RR	DET
KOH		NaCl	
	Ti CP2	0.0824	0.5542
	Ti-6Al-2Sn-4Zr-2Mo	0.0788	0.8378
	Ti-6Al-4V	0.5779	0.9962
	Ti Beta-C	0.3508	0.6901
		H <sub>2</sub> SO <sub>4</sub>	
	Ti CP2	0.3045	0.888
	Ti-6Al-2Sn-4Zr-2Mo	0.1421	0.9126
	Ti-6Al-4V	0.1105	0.4718
	Ti Beta-C	0.0829	0.8696

3.3. Electrochemical Impedance Spectroscopy

Electrochemical impedance spectroscopy (EIS) has been widely used to study the electrochemical mechanisms at electrodes. The characteristics of the EIS spectra of the samples investigated in the present study are presented in Figures 11–14; they show Nyquist and Bode plots for anodized titanium alloys immersed in 3.5 wt. % NaCl and H<sub>2</sub>SO<sub>4</sub> solution.

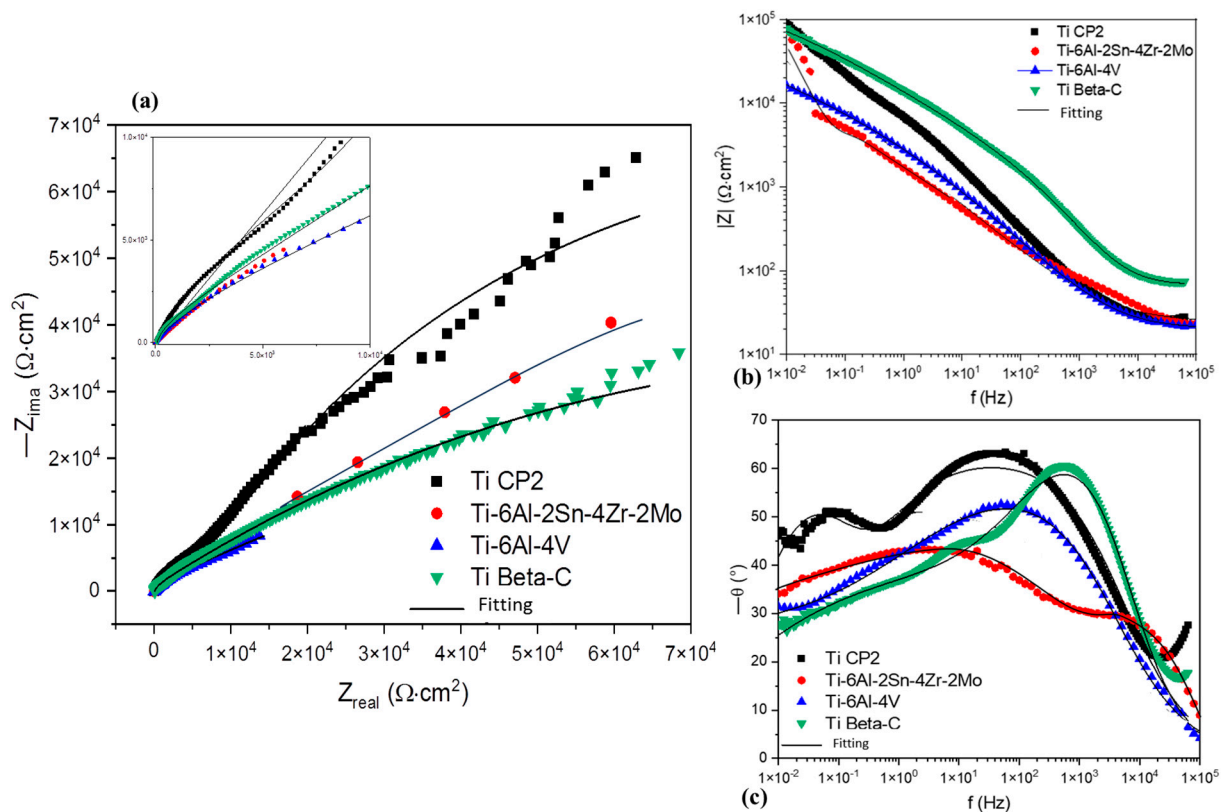


**Figure 11.** EIS of anodized titanium alloys in NaOH exposed in NaCl. (a) Nyquist, (b) Bode of  $|Z|$  vs. frequency, and (c) phase angle Bode.

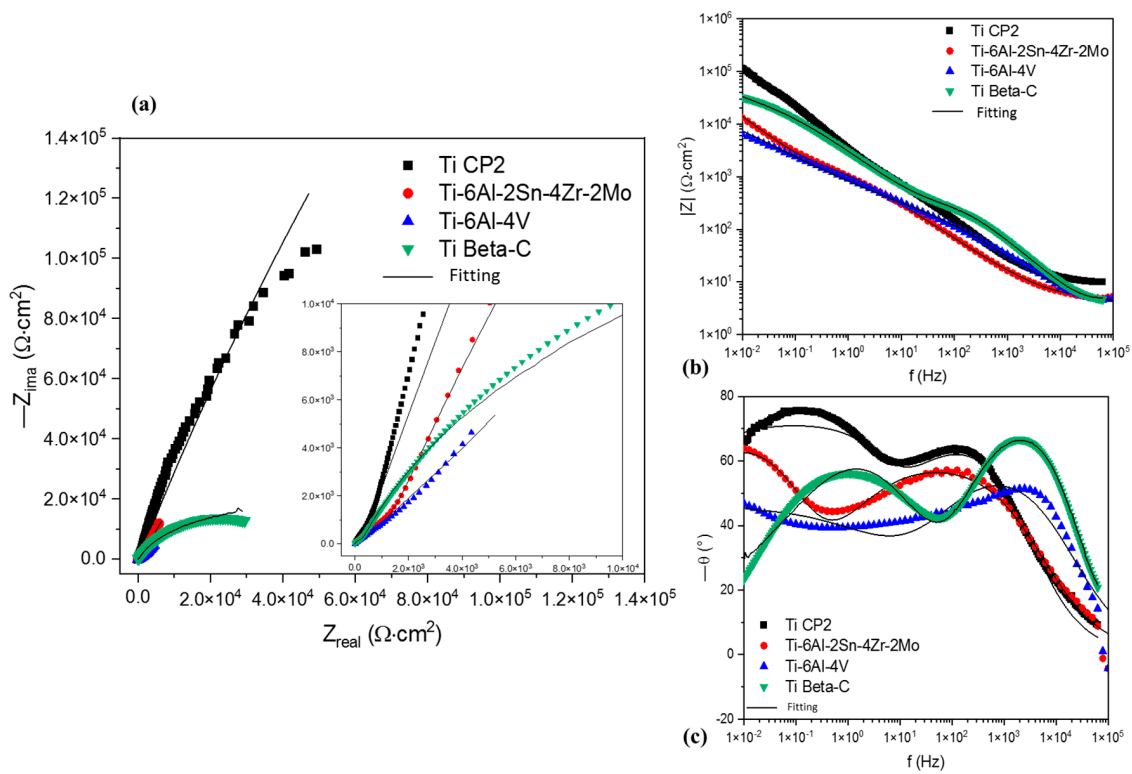


Figure 12. EIS of anodized titanium alloys in NaOH exposed in H<sub>2</sub>SO<sub>4</sub>. (a) Nyquist, (b) Bode of  $|Z|$  vs. frequency, and (c) phase angle Bode.

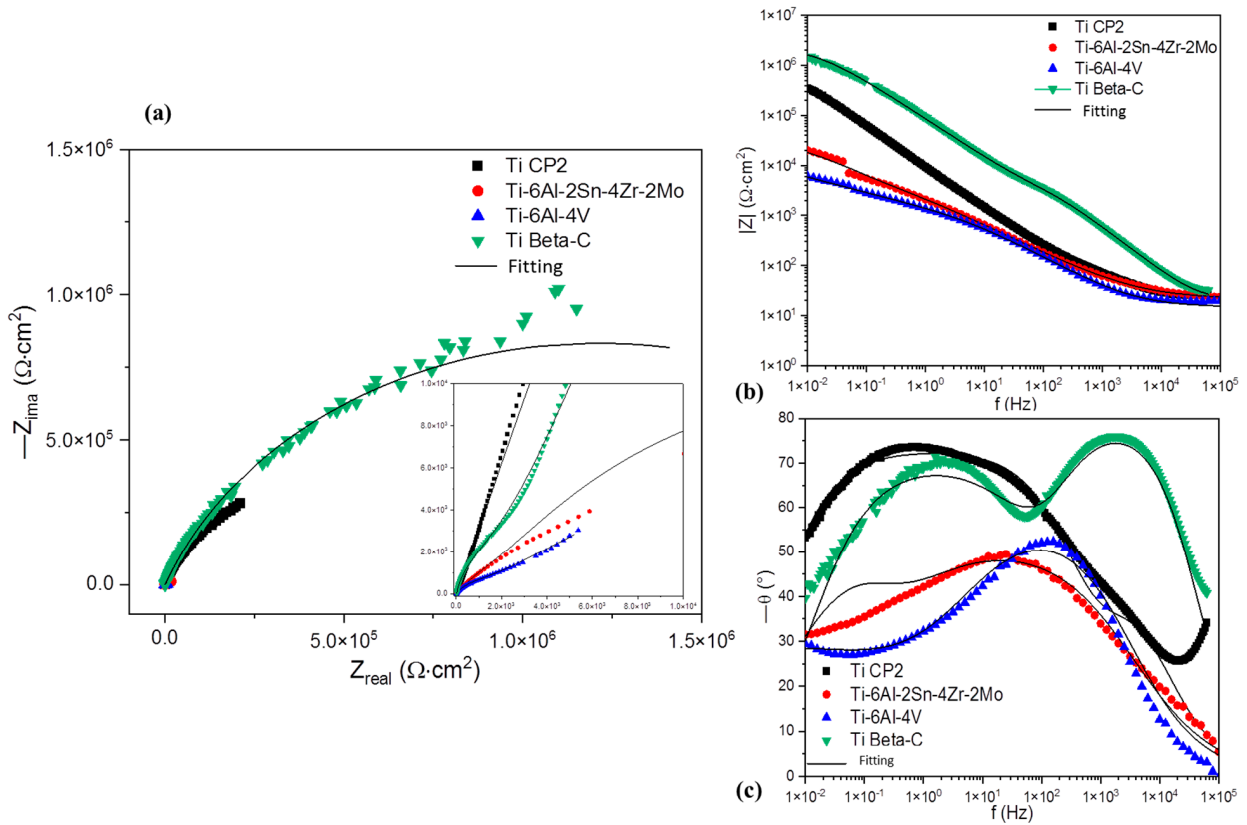
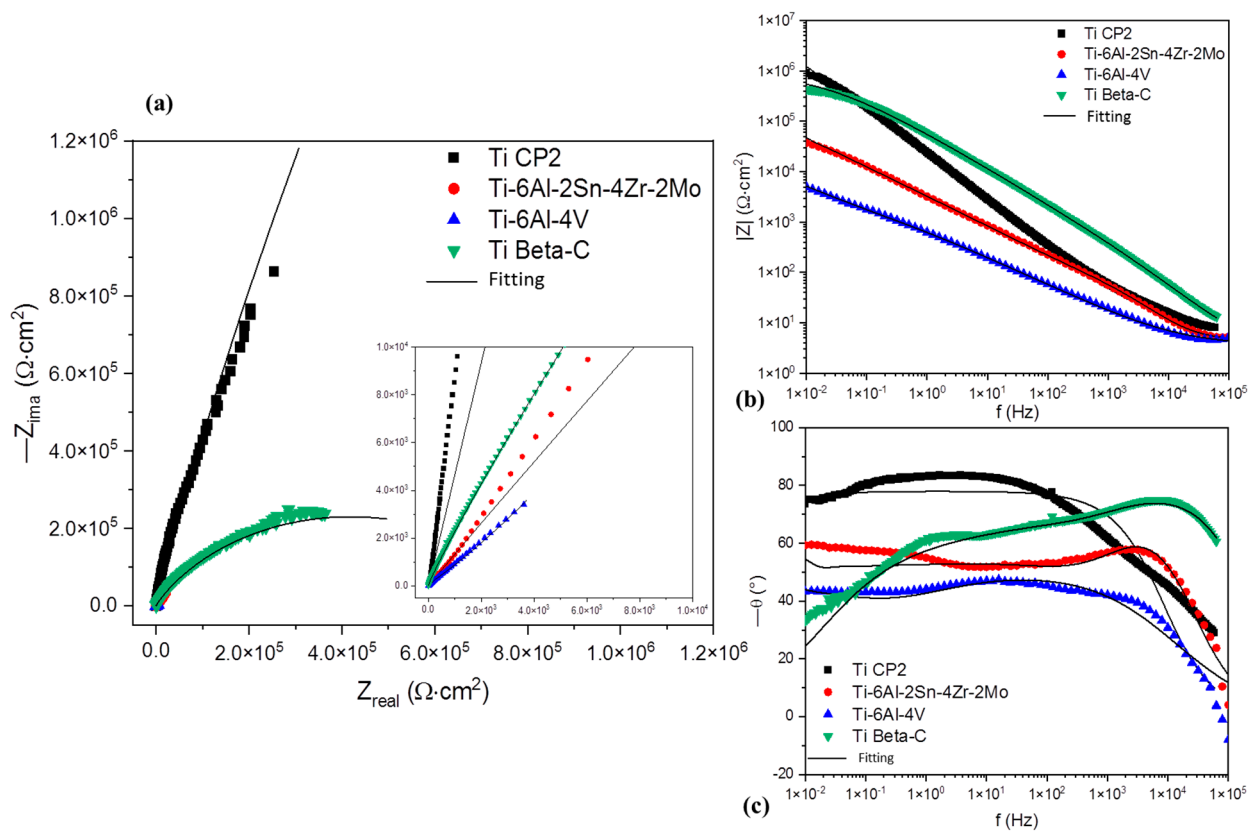


Figure 13. EIS of anodized titanium alloys in KOH exposed in NaCl. (a) Nyquist, (b) Bode of  $|Z|$  vs. frequency, and (c) phase angle Bode.





**Figure 14.** EIS of anodized titanium alloys in KOH exposed in  $\text{H}_2\text{SO}_4$ . (a) Nyquist, (b) Bode of  $|Z|$  vs. frequency, and (c) phase angle Bode.

Figure 11 shows Ti alloys anodized in NaOH exposed to NaCl. The anodized Ti CP2 showed a high resistance with  $2.4 \times 10^4 \Omega \cdot \text{cm}^2$ , and the lowest capacitance of  $3.37 \times 10^{-5}$  and  $4.75 \times 10^{-5} \text{ F/cm}^2$  (see Table 5). This behavior indicates that the layer of this anodized alloy presented acceptable properties against corrosion. The “ $n$ ” values for the anodized Ti CP2 are 0.7 and 0.8 in both high- and low-frequency interfaces, meaning there is a capacitive system predominance. On the other hand, the anodized Ti-6Al-4V and Ti Beta-C presented in the first have interface values of 0.8 and 0.7, respectively, indicating capacitive behavior in the first porous layer. However, in the second interface, the  $n$  values were 0.3 and 0.4, respectively, indicating more resistive behavior; the alloys acted as resistors rather than capacitors. This is associated with the high value of capacitance ( $1.27 \times 10^{-4}$  and  $3.16 \times 10^{-5} \text{ F/cm}^2$ ), which suggests a faster ionic dissolution process due to the heterogeneities on the surface.

**Table 5.** Parameters obtained by EIS for anodized titanium alloy samples.

Alloy	$R_s$ ( $\Omega \cdot \text{cm}^2$ )	$R_{\text{por}}$ ( $\Omega \cdot \text{cm}^2$ )	CPE-T ( $\text{F/cm}^2$ )	$n$	$R$ ( $\Omega \cdot \text{cm}^2$ )	CPE-T2 ( $\text{F/cm}^2$ )	$n$	$W$ ( $\Omega \cdot \text{cm}^2$ )	$\chi^2$
Ti CP2									
3.5% NaCl									
NaOH	19.1	$2.4 \times 10^4$	$3.37 \times 10^{-5}$	0.7	$1.72 \times 10^5$	$4.75 \times 10^{-5}$	0.8	-	0.01
KOH	20.3	92.4	$9.78 \times 10^{-6}$	0.8	$1.01 \times 10^6$	$1.36 \times 10^{-5}$	0.8	-	0.01

Table 5. Cont.

Alloy	Rs ( $\Omega \cdot \text{cm}^2$ )	R <sub>por</sub> ( $\Omega \cdot \text{cm}^2$ )	CPE-T (F/cm <sup>2</sup> )	n	R ( $\Omega \cdot \text{cm}^2$ )	CPE-T2 (F/cm <sup>2</sup> )	n	W ( $\Omega \cdot \text{cm}^2$ )	X <sup>2</sup>
3.5% H <sub>2</sub> SO <sub>4</sub>									
NaOH	9.8	1530	$4.29 \times 10^{-5}$	0.8	$2.41 \times 10^6$	$2.59 \times 10^{-5}$	0.8	-	$5 \times 10^{-3}$
KOH	9.1	$2.65 \times 10^7$	$8.92 \times 10^{-6}$	0.9	-	-	-	-	$5 \times 10^{-2}$
Ti-6Al-2Sn-4Zr-2Mo									
3.5% NaCl									
NaOH	21.3	$20.8 \times 10^3$	$1.47 \times 10^{-4}$	0.6	$18 \times 10^3$	$2.05 \times 10^{-4}$	0.8	-	$7 \times 10^{-4}$
KOH	21.8	8409	$1.34 \times 10^{-4}$	0.7	$2.88 \times 10^4$	$1.11 \times 10^{-4}$	0.7	-	$9 \times 10^{-3}$
3.5% H <sub>2</sub> SO <sub>4</sub>									
NaOH	4.5	2473	$1.96 \times 10^{-4}$	0.8	$3.15 \times 10^5$	$4.06 \times 10^{-4}$	0.8	-	$2 \times 10^{-3}$
KOH	4.6	83.5	$5.64 \times 10^{-6}$	-	-	-	-	$1.39 \times 10^5$	$6 \times 10^{-3}$
Ti-6Al-4V									
3.5% NaCl									
NaOH	20.1	1761	$6.55 \times 10^{-5}$	0.7	$7.85 \times 10^5$	$1.27 \times 10^{-4}$	0.3	-	$3 \times 10^{-4}$
KOH	14.8	1238	$9.34 \times 10^{-5}$	0.7	$1.12 \times 10^5$	$5.01 \times 10^{-4}$	0.4	-	$1 \times 10^{-2}$
3.5% H <sub>2</sub> SO <sub>4</sub>									
NaOH	3.7	296	$7.61 \times 10^{-5}$	0.7	-	-	-	$2.7 \times 10^4$	$1 \times 10^{-2}$
KOH	3.57	2158	$4.70 \times 10^{-4}$	0.6	-	-	-	$3.15 \times 10^4$	$7 \times 10^{-3}$
Ti Beta-C									
3.5% NaCl									
NaOH	66.9	1589	$2.11 \times 10^{-6}$	0.8	$2.1 \times 10^5$	$3.16 \times 10^{-5}$	0.4	-	$1 \times 10^{-3}$
KOH	20.7	5418	$6.23 \times 10^{-7}$	0.9	$2.43 \times 10^6$	$2.17 \times 10^{-6}$	0.7	-	$6 \times 10^{-3}$
3.5% H <sub>2</sub> SO <sub>4</sub>									
NaOH	4.1	284	$6.93 \times 10^{-6}$	0.9	$4.4 \times 10^4$	$8.94 \times 10^{-5}$	0.7	-	$1 \times 10^{-3}$
KOH	3.7	1201	$1.05 \times 10^{-7}$	0.9	$8.54 \times 10^5$	$4.31 \times 10^{-6}$	0.6	-	$1 \times 10^{-3}$

Figure 12 shows the results of samples anodized in NaOH exposed to H<sub>2</sub>SO<sub>4</sub>. The samples showed a similar trend to the samples exposed on NaCl, where the Nyquist and frequency vs. |Z| diagrams of Figure 12a,b show a high impedance module for anodized Ti CP2, as well as higher values of impedance in the Nyquist diagram. Ti Beta-C presented high values of resistance. On the other hand, Ti-6Al-4V presented a behavior associated with a diffusion system. The Warburg process can be observed in the windowing performed on the Nyquist diagram of Figure 12a and in the diagram of Figure 12c, where the phase angle finished at 45° at low frequencies, indicating that the diffusion process occurs at low frequencies. The Warburg resistance is  $2.7 \times 10^4 \Omega \cdot \text{cm}^2$ . At the same time, the first process presented a resistance of  $289 \Omega \cdot \text{cm}^2$  and a capacitance of  $7.61 \times 10^{-5} \text{ F/cm}^2$ , with an n value of 0.7. The first process is related to a capacitive system with a heterogeneous surface. Ti CP presented n values of 0.8 and 0.9, meaning that the distribution of ionic charges is more homogenous [35].

Figure 13 shows the samples anodized on KOH exposed to NaCl. In this medium, all the anodized alloys showed a double-layer behavior, where Ti Beta-C presented better performance against corrosion. Ti CP2 also presented good behavior against corrosion. Ti-6Al-4V presented the lower impedance values, with  $1238 \Omega \cdot \text{cm}^2$ , with n values of 0.7 and 0.4. This means that the surface is homogenous, and the process in the second layer

is predominantly resistive. Also, this indicates a dissolution process that occurs on the anodized surface.

Figure 14 shows the results of samples anodized in KOH exposed to H<sub>2</sub>SO<sub>4</sub>. Ti CP2 and Ti Beta-C alloys presented a higher impedance; however, Ti CP2 only presented a one-time variable. This behavior is related to a compact oxide layer due to the impedance value of  $2.65 \times 10^7 \Omega \cdot \text{cm}^2$  with a capacitance of  $8.92 \times 10^{-6} \text{ F/cm}^2$  and an  $n$  value of 0.9, indicating that the charges distribution is homogenous. On the other hand, Ti-6Al-4V and Ti-6Al-2Sn-4Zr-2Mo presented a diffusion process at low frequencies, indicating the dissolution of the oxide layer. The Warburg resistance of alloys is  $1.39 \times 10^9$  and  $3.15 \times 10^4 \Omega \cdot \text{cm}^2$ .

The table below shows the results of EIS parameters. The results were discussed in the diagram topic. The values of  $X^2$  are related to the error of fitting, meaning the values are lower and the fitting is better [36]. In this case, the value increases when, at high frequencies, the impedance is dispersed (the first four or five values).

The physical and mathematical model of the metal/anodized layer film/solution system is presented in Figure 15. The electrochemical impedance technique provides parameters such as solution resistance ( $R_s$ ), transference charge resistance ( $R_{ct}$ ), capacitance ( $C_{dl}$ ), constant phase element (CPE), or diffusion ( $W$ ), depending on the case [referencia nueva].

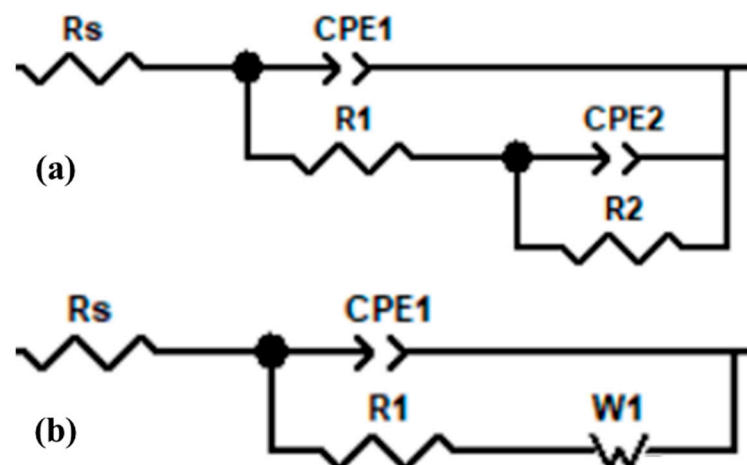


Figure 15. Equivalent circuits for (a) double-layer system and (b) Warburg's system.

The impedance of the system is obtained using the following equation [37]:

$$Z = \frac{E}{I} = Z_0 \exp(i\Phi) = Z_0(\cos\Phi + i\sin\Phi) \quad (7)$$

$Z$ ,  $E$ ,  $I$ ,  $\omega$ , and  $\Phi$  are the impedance, potential, current, frequency, and the phase angle between  $E$  and  $I$ .

Hence, the following equation can interpret the capacitance obtained by EIS measurements.

$$Z_c(\omega) = \frac{1}{i\omega C} \quad (8)$$

where  $C$  is the capacitance value; nevertheless, if the value of the capacitance is not close, it is possible that a CPE phenomenon is occurring in the system, and the equation that governs this is:

$$Z_{CPE}(\omega) = \frac{1}{(i\omega)^{\alpha} Q^{\alpha}} \quad (9)$$

where  $\alpha$  is a constant related to the uniform charge distribution and  $Q$  is the system's capacitance.



On the other hand, when a mass diffusion occurs in the system, a Warburg's element is possibly present on the equivalent circuits [38,39].

$$Z_w(\omega) = \sigma\omega^{-1/2} - i\left(\sigma\omega^{-\frac{1}{2}}\right) \quad (10)$$

#### 4. Discussion

The anodized NaOH noted in another paper was reported to have oxide-layer porosities of 0.1 to 1  $\mu\text{m}$ . This supports the idea that the percentage of porosity depends directly on the alloys' chemical composition [40]. Also, Afshar et al. [18] obtained anodized alloys with thicknesses from 0.4 to 1.5  $\mu\text{m}$ . They related the anodized time to the thickness of the oxide layer. In this research, the anodized thickness ranged from 23 nm to 2.63  $\mu\text{m}$ , where Ti-6Al-2Sn-4Zr-2Mo and Ti Beta-C presented higher thicknesses. Considering that the anodized parameters were the same for all experiments, the anodized thickness depends on the chemical composition of the alloy. Ti-6Al-4V generated an oxide layer of 23 nm related to the presence of V. However, Mo, Cr, and Zr alloys presented better oxide-layer generation.

When the KOH was employed as the anodized electrolyte, Burleigh et al. [41] obtained oxide layers of 300 nm; they concluded that NaOH and KOH are very similar in terms of generating oxide layers in Ti alloys. Hsu et al. [42] conducted research in which they anodized Ti-7.5 Mo in alkaline electrolytes and obtained a thin oxide layer with nanopores. The generation of the porosities was attributed to the penetration of  $\text{Na}^+$  and  $\text{OH}^-$  ions in the anodized surface, provoking a porous layer of sodium and hydroxide titanate ( $\text{Na}_x\text{H}_2\text{-xTi}_3\text{O}_7$ ) after exposition to the alkaline media. Due to the valence number of K, the surface reaction is very similar to the anodized NaOH.

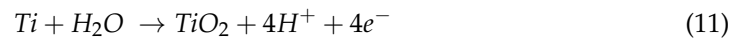
Laurindo et al. [43] related the size porosity increase to the thickness when the current density increases. However, this will create surface cracks. This occurs on anodized Ti Beta-C. Additionally, Zhang et al. [44] found that pore size depends on the ionic current anodized. Also, Mazzarolo et al. [45] conclude that an amorphous barrier is created on the Ti surface, making the alloy susceptible to generating oxide in preferential zones when small ions such as  $\text{Na}^+$  and  $\text{K}^+$  are deposited in specific zones and generate oxide in specific zones. This behavior was presented in this research.

It is important to mention that  $\text{Cl}^-$  acts as an interstitial element, so when the anodized has tiny pores or cracks, the ion penetrates the surface to attack [46].  $\text{Cl}^-$ 's presence induces localized corrosion because the ions attack the more susceptible zones. The accumulation of oxychlorides is expected to occur on the metal–oxide interface; this is due to the breaking of the oxide layer, and it provokes a localization process [47,48]. This occurs when the "n" of CPE values differ by 0.5, which is associated with the accumulation of  $\text{Cl}^-$  on the surface until they break the interface; this is the double-layer mechanism. The capacitance values obtained are related to the resistance or the opposition of ionic transference on the surface [49].

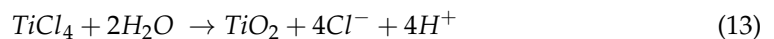
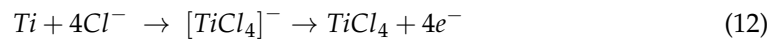
Song et al. [50] reported the effects of different Ti alloys exposed to saline media. They found that the alloys with V presented a lower corrosion resistance than the other alloys; this occurred due to the V oxide layer created in the corrosion process being dissolved faster than the other oxide layers. This behavior is presented in all Ti-6Al-4V alloys, with lower corrosion resistance. The corrosion resistance increased for alloys that showed Cr, Mo, or Zr. Also, the susceptibility to  $\text{Cl}^-$  can be observed on HHT specters when high energy is present at the middle and high frequencies.

A helpful technique is EIS for barrier systems. The values obtained on "n" are related to capacitive behavior (near to 1), the diffusive system (0.5), or the resistive system (less than 0.5) [51]. Gomes et al. [52] related the "n" value to the charge distribution on the oxide layer determined by the thickness. Also, authors such as Gateman [53] conclude that the CPE behavior is related to the interface system, and a correct analysis will depend on the knowledge of the system. Therefore, if "n" is a value of 1, the surface is homogenous. Still, a different value is associated with a heterogeneous surface.

For the cases that presented diffusion, the processes that govern the Warburg element are absorption, penetration, and diffusion. The absorption occurs in the porous zones, while the diffusion occurs in the more compact oxide zones. This can create a higher corrosion resistance when the diffuser elements generate another passive layer [54–57]. The basic chemical reactions that occur in diffusion are:



However, when the diffusion process begins in a saline environment, the  $Cl^-$  has an important role and changes the chemical reactions:



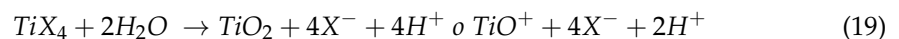
This behavior is very similar in all the aqueous solutions; independently of the composition, the hydrogen will react due to evolution, given by the next equation [58]:



This phenomenon occurs in cathodic reactions where hydrogen reacts. On the other hand, the growth of a passive layer in electrochemical conditions is represented by the next equations [59–61]:



The results show that the diffusion process on titanium and anodized alloys occurs in the solid state due to the ions' diffusion in the porous zone. The micropores from the first barrier act as diffusion zones [62–66]. That means the anodized alloys also have some corrosion resistance, so the  $Cl^-$  can break the protective barrier. Prando et al. [56] associated this behavior with the susceptibility of Ti to halides and proposed the next reaction:



X is a halide. When the solution does not have perturbation, water is the only transport for pitting the  $TiO_2$  and  $H^+$  out of the system. This permits the electrolyte to permeate the anodized breaking alloy and reduce the corrosion resistance. Additionally, elements such as Nb, Pd, and Cr increase the corrosion resistance, as occurs on Ti Beta-C.

On the other hand, when the electrolyte is  $H_2SO_4$ , the ions generate cathodic reactions, hydroxide diffusion, and passive layers. Therefore, the system with HHT and recurrence plots must be studied. The common behavior of anodization in this medium is the generation of an oxide layer that is broken and re-generated. Also,  $OH^-$  and  $SO_4^-$  generate unstable systems and generate cracks in anodized alloys [30,67].

Sadek et al. [59] mentioned that heterogeneities and susceptibility to localized attacks are due to the formation of hydroxides ( $Ti(OH)_xO_y$ ), as the hydroxides avoid the generation of an oxide layer. The porous barrier of the hydroxides generates the anodized diffusion process [68–73].

Also, when exposed to  $H_2SO_4$ , the reactions generate an oxide layer (diffusion). However, if the oxide is not solid, it will degrade. The diffusion process is blocked when the “n” values are 0.4 or 0.6. Authors Gonzalez, Pardave, Rodriguez, et al. [74–77] mentioned that when the “n” value is 0.4 and 0.6, the diffusion process is not perfect; it may signal trapped diffusion or blocked diffusion due to differences in surface quality. For that reason,

in this research, when the “n” value was not 0.5, we did not consider it diffusion. The next equation shows the behavior of a diffusion government process.

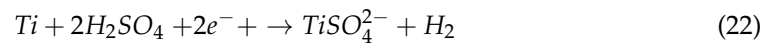
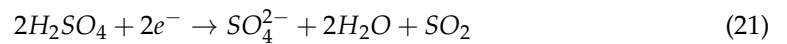
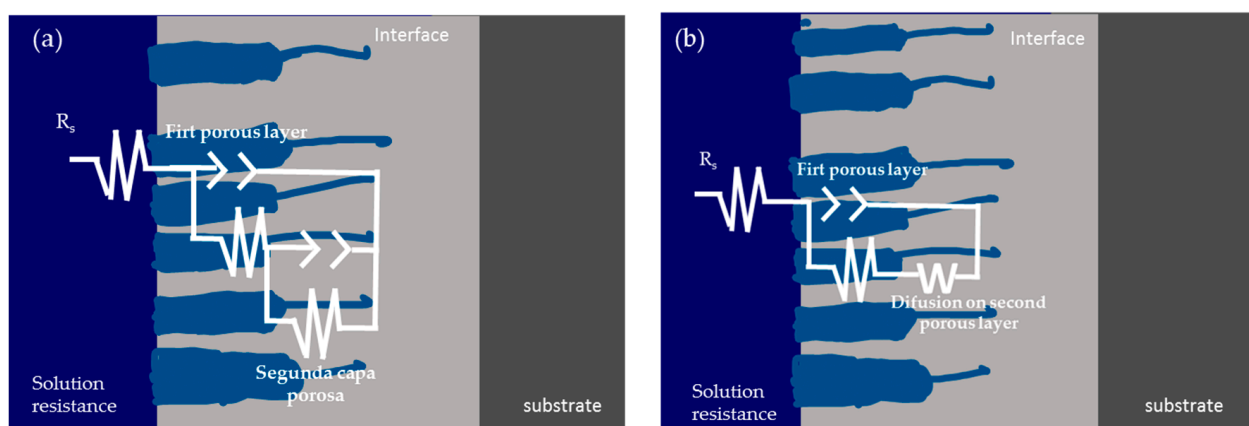


Figure 16 shows the equivalent circuit for the two different systems. Figure 16a shows the double-layer system, where the first resistance is related to the solution resistance, the second is with  $R_{ct}$  ( $R_{por}$ ), and the third is more linked with the double layer of oxide. The anodized alloys with less presence of  $\beta$  elements presented a higher  $R_{por}$  when anodized on NaOH than those with a high presence of  $\beta$  alloying elements, which presented higher  $R_{por}$  values when anodized in the KOH electrolyte.



**Figure 16.** Schematic of ECC for the two different models. (a) double-barrier system, (b) diffusion system.

Furthermore, the electrolyte of  $H_2SO_4$  trends to generate a diffusion process in the anodized Ti-6Al-2Sn-4Zr-2Mo and Ti-6Al-4V. In this last case, for anodized Ti-6Al-4V, the ECC showed  $n$  values of 0.4 and 0.3. This is controversial because some authors related it to a diffusion process and others to a resistive process. The physical value of “n” has been discussed by many authors. CPE is related to the conductive behavior of the dielectric. However, as the modeling is complex, it is difficult to determine the system. Moreover, the authors related the “n” value to factors such as roughness; if “n” has values from 1 to 0.9, it is governed by power law. However, if the value is from 0.5, it suggests a contorted surface, indicating Warburg diffusion. Also, the value of “n” is linked with the homogeneity of the surface and the variation in surface composition. For coatings, “n” values near 1 are related to uniform surfaces that present good anti-corrosion properties [78–84].

The second corrosion process is linked to another porous layer, so the scheme of Figure 16 is linked with two porous layers.

The use of recurrence plots in passive systems has been discussed because they present similar values to uniform corrosion. However, when the porosities increase, the determinism values decrease. This is due to the anodic–cathodic process that occurred on the surface; this is characteristic of passivation systems. The low determinism values occurred in anodized alloys with more corrosion resistance [85–89].

## 5. Conclusions

- The results indicated that the anodizing treatment on titanium alloys had a better effect when NaOH baths were used due to increased impedance, meaning greater corrosion resistance.



- The chemical composition of alloys is vital to generate a good, anodized alloy. The alloys with more  $\beta$  elements presented problems in generating a uniform oxide layer.
- Ti-6Al-4V presented more problems when generating a homogenous oxide layer due to the presence of V in the alloy. The generation of vanadium oxide made the anodized alloy susceptible to pitting attacks because the vanadium oxide has more interstitial spaces.
- The anodized alloys with fewer  $\beta$  elements (Ti CP2 and Ti-6Al-2Sn-4Zr-2Mo) presented higher  $R_{\text{por}}$  ( $R_{\text{ct}}$ ) resistance when anodized on NaOH. On the other hand, alloys with a high presence of  $\beta$  elements presented more anodized  $R_{\text{por}}$  ( $R_{\text{ct}}$ ) on KOH.
- Ti-6Al-4V presented a lower thickness, at 25 nm, when it was anodized in an NaOH bath.
- Ti Beta-C presented better activity against corrosion due to the presence of Cr in the alloy.
- The EN technique analyzed by HHT and RP helps determine the type of corrosion process that predominates in the electrochemical system. In this type of case, the use of EN is helpful for observing the behavior of the localization process due to the limitation of other techniques in evaluating systems that do not present uniform corrosion processes.
- Recurrence plots analysis showed that anodized alloys are more susceptible to pitting when exposed to NaCl media due to the vertical and horizontal reaction distribution. On the other hand, when exposed to  $\text{H}_2\text{SO}_4$ , the anodized alloys presented behavior related to passive and uniform systems.
- The EIS results indicated that Ti Beta-C presented better resistance against corrosion for obtained values of  $9.7 \times 10^7 \Omega \cdot \text{cm}^2$ . Also, the anodized KOH presented more impedance.
- The values of CPE for the anodized alloy in KOH are in the order of  $10^{-7}$  and  $10^{-6}$  ( $\text{F}/\text{cm}^2$ ), indicating low capacitance and a better performance against ionic transference.
- The  $\text{H}_2\text{SO}_4$  made the anodized alloys susceptible to present diffusion. However, NaCl can present more damage due to the generation of hydroxides and salts on the metal-coating interface.

**Author Contributions:** Conceptualization, F.A.-C., J.M.J.-M. and C.G.-T.; methodology, J.M.J.-M., D.N.-M., M.L.-B., M.Á.B.-Z., E.M.-B., M.A.L.-M., L.L.-R. and H.R.-B.; data curation, F.A.-C., J.M.J.-M., E.M.-B., D.N.-M.; M.L.-B., L.L.-R., H.R.-B., L.D.L.-L. and C.G.-T.; formal analysis, C.G.-T., M.Á.B.-Z., F.A.-C., L.D.L.-L. and J.M.J.-M.; writing—review and editing, F.A.-C., J.M.J.-M. and C.G.-T. All authors have read and agreed to the published version of the manuscript.

**Funding:** This research was funded by the Universidad Autónoma de Nuevo León (UANL).

**Data Availability Statement:** The original contributions presented in the study are included in the article, further inquiries can be directed to the corresponding authors.

**Acknowledgments:** The authors acknowledge The Academic Body UANL—CA-316 “Deterioration and integrity of composite materials”.

**Conflicts of Interest:** The authors declare no conflicts of interest.

## References

1. Gialanella, S.; Malandrucolo, A. *Aerospace Alloys*; Topics in Mining, Metallurgy and Materials Engineering; Springer International Publishing: Cham, Switzerland, 2020; ISBN 9783030244392.
2. Mouritz, A.P. *Introduction to Aerospace Materials*; Elsevier Inc.: Amsterdam, The Netherlands, 2012; ISBN 9781855739468.
3. Giurgutiu, V. Introduction. In *Structural Health Monitoring of Aerospace Composites*; Elsevier: Boston, MA, USA, 2016; pp. 1–23. [[CrossRef](#)]
4. Schweitzer, P.E. *PA Corrosion Engineering Handbook—3 Volume Set*; CRC Press: Boca Raton, FL, USA, 2018; ISBN 9780429188084.
5. Hebert, K.; Alkire, R. Dissolved Metal Species Mechanism for Initiation of Crevice Corrosion of Aluminum: II. Mathematical Model. *J. Electrochem. Soc.* **1983**, *130*, 1007–1014. [[CrossRef](#)]

6. Rashidi, N.; Alavi-Soltani, S.R.; Asmatulu, R. *Crevice Corrosion Theory, Mechanisms and Prevention Methods*; SOAR: Cambridge, UK, 2007.
7. Rodrigues, D.C.; Urban, R.M.; Jacobs, J.J.; Gilbert, J.L. In Vivo Severe Corrosion and Hydrogen Embrittlement of Retrieved Modular Body Titanium Alloy Hip-Implants. *J. Biomed. Mater. Res. B Appl. Biomater.* **2009**, *88*, 206–219. [[CrossRef](#)]
8. Zieliński, A.; Sobieszczyk, S. Corrosion of Titanium Biomaterials, Mechanisms, Effects and Modelisation. *Corros. Rev.* **2008**, *26*, 1–22. [[CrossRef](#)]
9. Pourbaix, M.; Burbank, J. Atlas D-Equilibres Electrochimiques. *J. Electrochem. Soc.* **1964**, *111*, 14C. [[CrossRef](#)]
10. Ono, S.; Ichinose, H.; Kawaguchi, T.; Masuko, N. The Observation of Anodic Oxide Films on Aluminum by High Resolution Electron Microscopy. *Corros. Sci.* **1990**, *31*, 249–254. [[CrossRef](#)]
11. Palibroda, E.; Marginean, P. Considerations on the Adsorbed Water Concentration of Sulfuric Porous Aluminium Oxide. *Thin Solid Film.* **1994**, *240*, 73–75. [[CrossRef](#)]
12. Voon, C.H.; Derman, M.N.; Hashim, U.; Ahmad, K.R.; Foo, K.L. Effect of Temperature of Oxalic Acid on the Fabrication of Porous Anodic Alumina from Al-Mn Alloys. *J. Nanomater.* **2013**, *2013*, 167047. [[CrossRef](#)]
13. Lee, W.; Park, S.J. Porous Anodic Aluminum Oxide: Anodization and Templated Synthesis of Functional Nanostructures. *Chem. Rev.* **2014**, *114*, 7487–7556. [[CrossRef](#)]
14. Salman, S.A.; Okido, M. Anodization of Magnesium (Mg) Alloys to Improve Corrosion Resistance. *Corros. Prev. Magnes. Alloys* **2013**, *8*, 197–231. [[CrossRef](#)]
15. Martínez-Viademonte, M.P.; Abrahami, S.T.; Hack, T.; Burchardt, M.; Terry, H. A Review on Anodizing of Aerospace Aluminum Alloys for Corrosion Protection. *Coatings* **2020**, *10*, 1106. [[CrossRef](#)]
16. Regonini, D.; Bowen, C.R.; Jaroenworarluck, A.; Stevens, R. A Review of Growth Mechanism, Structure and Crystallinity of Anodized TiO<sub>2</sub> Nanotubes. *Mater. Sci. Eng. R Rep.* **2013**, *74*, 377–406. [[CrossRef](#)]
17. Hugot-Le Goff, A. Structure of Very Thin TiO<sub>2</sub> Films Studied by Raman Spectroscopy with Interference Enhancement. *Thin Solid Film.* **1986**, *142*, 193–197. [[CrossRef](#)]
18. Afshar, A.; Vaezi, M.R. Anodizing of Titanium in NaOH Solution and Its Corrosion Resistance in PBS Physiologic Solution. *Sci. Iran.* **2003**, *10*, 361–366.
19. Jáquez-Muñoz, J.M.; Gaona-Tiburcio, C.; Chacón-Nava, J.; Cabral-Miramontes, J.; Nieves-Mendoza, D.; Maldonado-Bandala, E.M.; Delgado, A.D.; Flores-De Los Rios, J.P.; Bocchetta, P.; Almeraya-Calderón, F. Electrochemical Corrosion of Titanium and Titanium Alloys Anodized in H<sub>2</sub>SO<sub>4</sub> and H<sub>3</sub>PO<sub>4</sub> Solutions. *Coatings* **2022**, *12*, 325. [[CrossRef](#)]
20. AMS2487B; Anodic Treatment of Titanium and Titanium Alloys Solution PH 12.4 Maximum. SAE: Warrendale, PA, USA, 2018; pp. 1–7.
21. AMS2488E; Anodic Treatment-Titanium and Titanium Alloys, Solution PH 13 or Higher. SAE International: Warrendale, PA, USA, 2019. Available online: <https://www.sae.org/standards/content/ams2488e/?src=ams2487b> (accessed on 23 June 2023).
22. ASTM E407-07; Standard Practice for Microetching Metals and Alloys. ASTM International: West Conshohocken, PA, USA, 2007.
23. ASTM G106-03; Standard Practice for Verification of Algorithm and Equipment for Electrochemical Impedance Measurements. ASTM International: West Conshohocken, PA, USA, 1999.
24. ASTM G199-09; Standard Guide for Electrochemical Noise Measurement. ASTM International: West Conshohocken, PA, USA, 2020.
25. Bertocci, U.; Huet, F. Noise Analysis Applied to Electrochemical Systems. *Corrosion* **1995**, *51*, 131–144. [[CrossRef](#)]
26. Coakley, J.; Vorontsov, V.A.; Littrell, K.C.; Heenan, R.K.; Ohnuma, M.; Jones, N.G.; Dye, D. Nanoprecipitation in a Beta-Titanium Alloy. *J. Alloys Compd.* **2015**, *623*, 146–156. [[CrossRef](#)]
27. Cai, C.; Zhang, Z.; Cao, F.; Gao, Z.; Zhang, J.; Cao, C. Analysis of Pitting Corrosion Behavior of Pure Al in Sodium Chloride Solution with the Wavelet Technique. *J. Electroanal. Chem.* **2005**, *578*, 143–150. [[CrossRef](#)]
28. Hai, L.; Guo-qiang, X.; Pan, Z.; Hua-sen, Z.; Khan, M.Y. The Hilbert–Huang Transform-Based Denoising Method for the TEM Response of a PRBS Source Signal. *Pure Appl. Geophys.* **2016**, *173*, 2777–2789. [[CrossRef](#)]
29. Zhang, Z.; Zhao, Z.; Bai, P.; Li, X.; Liu, B.; Tan, J.; Wu, X. In-Situ Monitoring of Pitting Corrosion of AZ31 Magnesium Alloy by Combining Electrochemical Noise and Acoustic Emission Techniques. *J. Alloys Compd.* **2021**, *878*, 160334. [[CrossRef](#)]
30. Homborg, A.M.; Tinga, T.; Van Westing, E.P.M.; Zhang, X.; Ferrari, G.M.; De Wit, J.H.W.; Mol, J.M.C. A Critical Appraisal of the Interpretation of Electrochemical Noise for Corrosion Studies. *Corrosion* **2014**, *70*, 971–987. [[CrossRef](#)] [[PubMed](#)]
31. Marwan, N.; Carmen Romano, M.; Thiel, M.; Kurths, J. Recurrence Plots for the Analysis of Complex Systems. *Phys. Rep.* **2007**, *438*, 237–329. [[CrossRef](#)]
32. Acuña-González, N.; García-Ochoa, E.; González-Sánchez, J. Assessment of the Dynamics of Corrosion Fatigue Crack Initiation Applying Recurrence Plots to the Analysis of Electrochemical Noise Data. *Int. J. Fatigue* **2008**, *30*, 1211–1219. [[CrossRef](#)]
33. Mayorga-Cruz, D.; Sarmiento-Martinez, O.; Menchaca Campos, C.; Uruchurtu, J. Analysis of Michelson Optical Interferometry Using Recurrence Plots During Corrosion of Aluminium in NaCl Solution. *ECS Trans.* **2009**, *20*, 433–446. [[CrossRef](#)]
34. Jirón-Lazos, U.; Corvo, F.; De la Rosa, S.C.; García-Ochoa, E.M.; Bastidas, D.M.; Bastidas, J.M. Localized Corrosion of Aluminum Alloy 6061 in the Presence of *Aspergillus Niger*. *Int. Biodeterior. Biodegrad.* **2018**, *133*, 17–25. [[CrossRef](#)]
35. Luo, Z.; Zhang, Y.; Wang, H.; Wan, S.; Song, L.; Liao, B.; Guo, X. Modified nano-lignin as a novel biomass-derived corrosion inhibitor for enhanced corrosion resistance of carbon steel. *Corros. Sci.* **2024**, *227*, 111705. [[CrossRef](#)]

36. Zhou, F.; Ma, Y.; Chen, Y.; Zhang, L.; Sheng, X. Triple-function smart anticorrosion composite coating based on graphene and ZIF-8 with excellent pH-responsive self-healing and in vitro antimicrobial properties. *Prog. Org. Coat.* **2024**, *186*, 108007. [[CrossRef](#)]
37. Magar, H.S.; Hassan, R.Y.A.; Mulchandani, A. Electrochemical Impedance Spectroscopy (EIS): Principles, Construction, and Biosensing Applications. *Sensors* **2021**, *21*, 6578. [[CrossRef](#)]
38. Orazem, M.E.; Tribollet, B. Constant-Phase Elements. In *Electrochemical Impedance Spectroscopy*; Wiley: Hoboken, NJ, USA, 2017; pp. 395–419.
39. Harrington, D.A.; Van Den Driessche, P. Mechanism and Equivalent Circuits in Electrochemical Impedance Spectroscopy. *Electrochim. Acta* **2011**, *56*, 8005–8013. [[CrossRef](#)]
40. Peixoto Barbosa, D.; Knörnschild, G. Anodization of Mg-Alloy AZ91 in NaOH Solutions. *Surf. Coat. Technol.* **2009**, *203*, 1629–1636. [[CrossRef](#)]
41. Burleigh, T.D.; Dotson, T.C.; Dotson, K.T.; Gabay, S.J.; Sloan, T.B.; Ferrell, S.G. Anodizing Steel in KOH and NaOH Solutions. *J. Electrochem. Soc.* **2007**, *154*, C579. [[CrossRef](#)]
42. Hsu, H.C.; Hsu, S.K.; Wu, S.C.; Hung, Y.H.; Ho, W.F. Surface Modification of Nanotubular Anodized Ti–7.5Mo Alloy Using NaOH Treatment for Biomedical Application. *Thin Solid Film.* **2020**, *710*, 138273. [[CrossRef](#)]
43. Laurindo, C.A.H.; Torres, R.D.; Mali, S.A.; Gilbert, J.L.; Soares, P. Incorporation of Ca and P on Anodized Titanium Surface: Effect of High Current Density. *Mater. Sci. Eng. C* **2014**, *37*, 223–231. [[CrossRef](#)] [[PubMed](#)]
44. Zhang, Y.; Fan, H.; Ding, X.; Yan, Q.; Wang, L.; Ma, W. Simulation of Anodizing Current-Time Curves and Morphology Evolution of TiO<sub>2</sub> Nanotubes Anodized in Electrolytes with Different NH<sub>4</sub>F Concentrations. *Electrochim. Acta* **2015**, *176*, 1083–1091. [[CrossRef](#)]
45. Mazarolo, A.; Curioni, M.; Vincenzo, A.; Skeldon, P.; Thompson, G.E. Anodic Growth of Titanium Oxide: Electrochemical Behaviour and Morphological Evolution. *Electrochim. Acta* **2012**, *75*, 288–295. [[CrossRef](#)]
46. Lee, C.C.; Mansfeld, F. Analysis of Electrochemical Noise Data for a Passive System in the Frequency Domain. *Corros. Sci.* **1998**, *40*, 959–962. [[CrossRef](#)]
47. Xia, D.H.; Song, S.Z.; Behnamian, Y. Detection of Corrosion Degradation Using Electrochemical Noise (EN): Review of Signal Processing Methods for Identifying Corrosion Forms. *Corros. Eng. Sci. Technol.* **2016**, *51*, 527–544. [[CrossRef](#)]
48. Xia, D.H.; Qin, Z.; Song, S.; Macdonald, D.; Luo, J.L. Combating Marine Corrosion on Engineered Oxide Surface by Repelling, Blocking and Capturing Cl<sup>-</sup>: A Mini Review. *Corros. Commun.* **2021**, *2*, 1–7. [[CrossRef](#)]
49. Pan, C.; Wang, X.; Behnamian, Y.; Wu, Z.; Qin, Z.; Xia, D.H.; Hu, W. Monododecyl Phosphate Film on LY12 Aluminum Alloy: PH-Controlled Self-Assembly and Corrosion Resistance. *J. Electrochem. Soc.* **2020**, *167*, 161510. [[CrossRef](#)]
50. Song, H.J.; Kim, M.K.; Jung, G.C.; Vang, M.S.; Park, Y.J. The Effects of Spark Anodizing Treatment of Pure Titanium Metals and Titanium Alloys on Corrosion Characteristics. *Surf. Coat. Technol.* **2007**, *201*, 8738–8745. [[CrossRef](#)]
51. Fouda, M.E.; Allagui, A.; Elwakil, A.S.; Das, S.; Psychalinos, C.; Radwan, A.G. Non-linear Charge-Voltage Relationship in Constant Phase Element. *AEU Int. J. Electron. Commun.* **2020**, *117*, 153104. [[CrossRef](#)]
52. Gomes, M.P.; Costa, I.; Pèbère, N.; Rossi, J.L.; Tribollet, B.; Vivier, V. On the Corrosion Mechanism of Mg Investigated by Electrochemical Impedance Spectroscopy. *Electrochim. Acta* **2019**, *306*, 61–70. [[CrossRef](#)]
53. Gateman, S.M.; Gharbi, O.; Gomes de Melo, H.; Ngo, K.; Turmine, M.; Vivier, V. *On the Use of a Constant Phase Element (CPE) in Electrochemistry*; Elsevier: Amsterdam, The Netherlands, 2022; Volume 36, p. 101133.
54. Martínez-Aparicio, B.; Martínez-Bastidas, D.; Gaona-Tiburcio, C.; Martín, U.; Cabral-Miramontes, J.; Almeraya-Calderón, F. Localized corrosion of 15–5 PH and 17–4 PH stainless steel in NaCl solution. *J. Solid State Electrochem.* **2023**, *27*, 2993–3001. [[CrossRef](#)]
55. Rajan, S.T.; VV, A.T.; Terada-Nakaishi, M.; Chen, P.; Hanawa, T.; Nandakumar, A.K.; Subramanian, B. Zirconium-Based Metallic Glass and Zirconia Coatings to Inhibit Bone Formation on Titanium. *Biomed. Mater.* **2020**, *15*, 065019. [[CrossRef](#)]
56. Radovanović, M.B.; Tasić, Ž.Z.; Simonović, A.T.; Petrović Mihajlović, M.B.; Antonijević, M.M. Corrosion Behavior of Titanium in Simulated Body Solutions with the Addition of Biomolecules. *ACS Omega* **2020**, *5*, 12768–12776. [[CrossRef](#)]
57. Almeraya-Calderón, F.; Jáquez-Muñoz, J.M.; Maldonado-Bandala, E.; Cabral-Miramontes, J.; Nieves-Mendoza, D.; Olgui-Coca, J.; Lopez-Leon, L.D.; Estupiñán-López, F.; Lira-Martínez, A.; Gaona Tiburcio, C. Corrosion Resistance of Titanium Alloys Anodized in Alkaline Solutions. *Metals* **2023**, *13*, 1510. [[CrossRef](#)]
58. Dubent, S.; Mazard, A. Characterization and corrosion behaviour of grade 2 titanium used in electrolyzers for hydrogen production. *Int. J. Hydrogen Energy* **2019**, *44*, 15622–15633. [[CrossRef](#)]
59. Escrivá-Cerdán, C.; Blasco-Tamarit, E.; García-García, D.M.; Akid, R.; Walton, J. Effect of temperature on passive film formation of UNS N08031 Cr-Ni alloy in phosphoric acid contaminated with different aggressive anions. *Electrochim. Acta* **2013**, *111*, 552–561. [[CrossRef](#)]
60. Liu, C.; Leyland, A.; Bi, Q.; Matthews, A. Corrosion resistance of multi-layered plasma-assisted physical vapour deposition TiN and CrN coatings. *Surf. Coat. Technol.* **2001**, *141*, 164–173. [[CrossRef](#)]
61. Balla, A.; Marcu, C.; Axante, D.; Borodi, G.; Lazar, D. Catalytic reduction of sulfuric acid to sulfur dioxide. *Cent. Eur. J. Chem.* **2012**, *10*, 1817–1823. [[CrossRef](#)]
62. Vasilescu, C.; Drob, S.I.; Osiceanu, P.; Moreno, J.M.C.; Prodana, M.; Ionita, D.; Demetrescu, I.; Marcu, M.; Popovici, I.A.; Vasilescu, E. Microstructure, Surface Characterization, and Electrochemical Behavior of New Ti-Zr-Ta-Ag Alloy in Simulated Human Electrolyte. *Metall. Mater. Trans. A Phys. Metall. Mater. Sci.* **2017**, *48*, 513–523. [[CrossRef](#)]

63. Munirathinam, B.; Neelakantan, L. Titania Nanotubes from Weak Organic Acid Electrolyte: Fabrication, Characterization and Oxide Film Properties. *Mater. Sci. Eng. C* **2015**, *49*, 567–578. [[CrossRef](#)] [[PubMed](#)]
64. Cui, W.F.; Jin, L.; Zhou, L. Surface Characteristics and Electrochemical Corrosion Behavior of a Pre-Anodized Microarc Oxidation Coating on Titanium Alloy. *Mater. Sci. Eng. C* **2013**, *33*, 3775–3779. [[CrossRef](#)] [[PubMed](#)]
65. Sun, J.; Liu, Y. Unique Constant Phase Element Behavior of the Electrolyte–Graphene Interface. *Nanomaterials* **2019**, *9*, 923. [[CrossRef](#)]
66. Prando, D.; Nicolis, D.; Pedferri, M.P.; Ormellese, M. Pitting Corrosion on Anodized Titanium: Effect of Halides. *Mater. Corros.* **2018**, *69*, 1441–1446. [[CrossRef](#)]
67. Fattah-Alhosseini, A.; Attarzadeh, F.R.; Vakili-Azghandi, M. Effect of Multi-Pass Friction Stir Processing on the Electrochemical and Corrosion Behavior of Pure Titanium in Strongly Acidic Solutions. *Metall. Mater. Trans. A Phys. Metall. Mater. Sci.* **2017**, *48*, 403–411. [[CrossRef](#)]
68. Sadek, A.Z.; Zheng, H.; Latham, K.; Wlodarski, W.; Kalantar-Zadeh, K. Anodization of Ti Thin Film Deposited on ITO. *Langmuir* **2009**, *25*, 509–514. [[CrossRef](#)]
69. Mor, G.K.; Varghese, O.K.; Paulose, M.; Mukherjee, N.; Grimes, C.A. Fabrication of Tapered, Conical-Shaped Titania Nanotubes. *J. Mater. Res.* **2003**, *18*, 2588–2593. [[CrossRef](#)]
70. Galván-Martínez, R.; Cabrera-de la Cruz, D.; Contreras, A.; Orozco-Cruz, R. A Novel Experimental Arrangement for Corrosion Study of X60 Pipeline Steel Weldments at Turbulent Flow Conditions. *Corros. Eng. Sci. Technol.* **2016**, *51*, 400–407. [[CrossRef](#)]
71. Galvan-Martinez, R.; Orozco-Cruz, R.; Torres-Sanchez, R.; Martinez, E.A. Corrosion Study of the X52 Steel Immersed in Seawater with a Corrosion Inhibitor Using a Rotating Cylinder Electrode. *Mater. Corros.* **2010**, *61*, 872–876. [[CrossRef](#)]
72. Chávez-Díaz, M.P.; Luna-Sánchez, R.M.; Vazquez-Arenas, J.; Lartundo-Rojas, L.; Hallen, J.M.; Cabrera-Sierra, R. XPS and EIS Studies to Account for the Passive Behavior of the Alloy Ti-6Al-4V in Hank’s Solution. *J. Solid State Electrochem.* **2019**, *23*, 3187–3196. [[CrossRef](#)]
73. Xia, D.-H.; Song, S.; Behnamian, Y.; Hu, W.; Cheng, Y.F.; Luo, J.-L.; Huet, F. Review—Electrochemical Noise Applied in Corrosion Science: Theoretical and Mathematical Models towards Quantitative Analysis. *J. Electrochem. Soc.* **2020**, *167*, 081507. [[CrossRef](#)]
74. Scharifker, B.K.; Monstany, J.; Palomar-Pardave, M.; González, I. On the Theory of the Potentiostatic Current Transient for Diffusion-Controlled Three-Dimensional Electrocrystallization Processes. *J. Electrochem. Soc.* **1999**, *146*, 1005. [[CrossRef](#)]
75. Gil, A.; Galicia, L.; González, I. Diffusion coefficients and electrode kinetic parameters of different Fe(III)-sulfate complexes. *J. Electroanal. Chem.* **1996**, *417*, 129–134. [[CrossRef](#)]
76. Cabrera-Sierra, R.; Hallen, J.M.; Vazquez-Arenas, J.; Vázquez, G.; González, I. EIS characterization of tantalum and niobium oxide films based on a modification of the point defect model. *J. Electroanal. Chem.* **2010**, *638*, 51–58. [[CrossRef](#)]
77. Rivero, E.P.; Rodríguez, F.A.; Cruz-Díaz, M.R.; González, I. Reactive diffusion migration layer and mass transfer wall function to model active chlorine generation in a filter press type electrochemical reactor for organic pollutant degradation. *Chem. Eng. Resear. Des.* **2018**, *138*, 533–545. [[CrossRef](#)]
78. Barsoukov, E.; Macdonald, J.R. *Impedance Spectroscopy: Theory, Experiment, and Applications*, 3rd ed.; John Wiley & Sons, Inc.: New York, NY, USA, 2018; pp. 175–478.
79. Macdonald, J.R. Frequency response of inifield dielectric and conductive systems involving an exponential distribution of activation energy. *J. Appl. Phys.* **1985**, *58*, 1955. [[CrossRef](#)]
80. Macdonald, J.R. Generalizations of “universal dielectric response” and a general distribution-of-activation-energies model for dielectric and conductive systems. *J. App. Phys.* **1985**, *58*, 1971. [[CrossRef](#)]
81. Mulder, W.H.; Sluyters, J.H.; Pajkossy, T.; Nyikos, L. Tafel current at fractal electrodes: Connection with admittance spectra. *J. Electroanal. Chem.* **1990**, *285*, 103. [[CrossRef](#)]
82. Kim, C.; Pyun, S.; Kim, J. An investigation of the capacitance dispersion on the fractal carbon electrode with edge and basal orientations. *Electrochim. Act.* **2003**, *48*, 3455. [[CrossRef](#)]
83. Schiller, C.A.; Strunz, W. The evaluation of experimental dielectric data of barrier coatings by means of different models. *Electrochim. Act.* **2001**, *46*, 3619. [[CrossRef](#)]
84. Córdoba-Torres, P. Relationship between constant-phase element (CPE) parameters and physical properties of films with a distributed resistivity. *Electrochim. Act.* **2017**, *225*, 592. [[CrossRef](#)]
85. Jáquez-Muñoz, J.M.; Gaona-Tiburcio, C.; Cabral-Miramontes, J.; Nieves-Mendoza, D.; Maldonado-Bandala, E.; Olguín-Coca, J.; López-Léon, L.D.; De Los Rios, J.P.F.; Almeraya-Calderón, F. Electrochemical Noise Analysis of the Corrosion of Titanium Alloys in NaCl and H<sub>2</sub>SO<sub>4</sub> Solutions. *Metals* **2021**, *11*, 105. [[CrossRef](#)]
86. Du, X.Q.; Yang, Q.S.; Chen, Y.; Yang, Y.; Zhang, Z. Galvanic Corrosion Behavior of Copper/Titanium Galvanic Couple in Artificial Seawater. *Trans. Nonferrous Met. Soc. China* **2014**, *24*, 570–581. [[CrossRef](#)]
87. Martínez-Villafañe, A.; Almeraya-Calderón, M.F.; Gaona-Tiburcio, C.; Gonzalez-Rodriguez, J.G.; Porcayo-Calderón, J. High-Temperature Degradation and Protection of Ferritic and Austenitic Steels in Steam Generators. *J. Mater. Eng. Perform* **1998**, *7*, 108–113. [[CrossRef](#)]



88. Gaona-Tiburcio, C.; Ramirez, A.; Gonzalez-Rodriguez, J.; Campillo, B. An Electrochemical Study of the Corrosion Behavior of a Dual Phase Steel in 0.5 m H<sub>2</sub>SO<sub>4</sub>. *Int. J. Electrochem. Sci.* **2010**, *5*, 1786.
89. Martínez-Ramos, C.; Olguín-Coca, J.; Lopez-Leon, L.D.; Gaona-Tiburcio, C.; Lara-Banda, M.; Maldonado-Bandala, E.; Castañeda-Robles, I.; Jaquez-Muñoz, J.M.; Cabral-Miramontes, J.; Nieves-Mendoza, D.; et al. Electrochemical Noise Analysis Using Experimental Chaos Theory, Power Spectral Density and Hilbert–Huang Transform in Anodized Aluminum Alloys in Tartaric–Phosphoric–Sulfuric Acid Solutions. *Metals* **2023**, *13*, 1850. [[CrossRef](#)]

**Disclaimer/Publisher’s Note:** The statements, opinions and data contained in all publications are solely those of the individual author(s) and contributor(s) and not of MDPI and/or the editor(s). MDPI and/or the editor(s) disclaim responsibility for any injury to people or property resulting from any ideas, methods, instructions or products referred to in the content.